Bioactive Materials 45 (2025) 322–344

Contents lists available at ScienceDirect

Bioactive Materials

journal homepage: www.keaipublishing.com/en/journals/bioactive-materials

An active shrinkage and antioxidative hydrogel with biomimetic mechanics functions modulates inflammation and fibrosis to promote skin regeneration

Tao Zhang [a,1], Xin-Cao Zhong [a,1], Zi-Xuan Feng [a,1], Xiao-Ying Lin [a], Chun-Ye Chen [a], Xiao-Wei Wang [a], Kai Guo [a], Yi Wang [a], Jun Chen [a,c], Yong-Zhong Du [a,b], Ze-Ming Zhuang [a,**], Yong Wang [a,***], Wei-Qiang Tan [a,*]

[a] Department of Plastic Surgery, Sir Run Run Shaw Hospital, Zhejiang University School of Medicine, 3 East Qingchun Road, Hangzhou, 310016, China
[b] Institute of Pharmaceutics, College of Pharmaceutical Sciences, Zhejiang University, 866 Yu-Hang-Tang Road, Hangzhou, 310058, China
[c] MOE Key Laboratory of Biosystems Homeostasis & Protection, College of Life Sciences, Zhejiang University, Hangzhou, 310058, China

ARTICLE INFO

Keywords:
Active shrinkage and antioxidative hydrogel
Biomimetic mechanics
ACEI microspheres
Anti-inflammation and anti-fibrosis
Skin regeneration

ABSTRACT

Achieving scar-free skin regeneration in clinical settings presents significant challenges. Key issues such as the imbalance in macrophage phenotype transition, delayed re-epithelialization, and excessive proliferation and differentiation of fibroblasts hinder wound healing and lead to fibrotic repair. To these, we developed an active shrinkage and antioxidative hydrogel with biomimetic mechanical functions (P&G@LMs) to reshape the healing microenvironment and effectively promote skin regeneration. The hydrogel's immediate hemostatic effect initiated sequential remodeling, the active shrinkage property sealed and contracted the wound at body temperature, and the antioxidative function eliminated ROS, promoting re-epithelialization. The spatiotemporal release of LMs (ACEI) during the inflammation phase regulated macrophage polarization towards the anti-inflammatory M2 phenotype, promoting progression to the proliferation phase. However, the profibrotic niche of macrophages induced a highly contractile α-SMA positive state in myofibroblasts, whereas the sustained LMs release could regulate this niche to control fibrosis and promote the correct biomechanical orientation of collagen. Notably, the biomimetic mechanics of the hydrogel mimicked the contraction characteristics of myofibroblasts, and the skin-like elastic modulus could accommodate the skin dynamic changes and restore the mechanical integrity of wound defect, partially substituting myofibroblasts' mechanical role in tissue repair. This study presents an innovative strategy for skin regeneration.

1. Introduction

Skin serves as the body's outer protective barrier, covering vital internal organs. Any deep damage, such as trauma, burns, or medical procedures, can lead to an overcorrection in the wound healing process, resulting in abnormal collagen production and arrangement, forming permanent scars [1,2]. Even with early wound closure through suturing, the lack of control over the internal microenvironment of the wound inevitably leads to scarring. Current research on promoting scar-free skin regeneration primarily focuses on the combined use of regenerative matrices and engineered cells with lower fibrogenic potential to modulate the healing environment [3,4], but ethical issues and high costs limit their application. Meanwhile, existing scar treatment methods such as surgery, radiation, and drug injections are costly and offer limited effectiveness [5,6], and there is a lack of intervention throughout the entire healing process. Typically, wound healing can be divided into four stages: hemostasis, inflammation, proliferation, and remodeling. After vascular damage, integrin receptors on platelets

Peer review under responsibility of KeAi Communications Co., Ltd.
* Corresponding author.
** Corresponding author.
*** Corresponding author.
E-mail addresses: 12218001@zju.edu.cn (Z.-M. Zhuang), wongyong@zju.edu.cn (Y. Wang), tanweixxxx@zju.edu.cn (W.-Q. Tan).
[1] These authors contributed equally to this work.

https://doi.org/10.1016/j.bioactmat.2024.11.028
Received 30 August 2024; Received in revised form 4 November 2024; Accepted 20 November 2024

recognize and bind to the arginine-glycine-aspartic acid (RGD) sequence in fibrinogen, activating platelets and causing them to crosslink, forming a thrombus to achieve hemostasis [7]. After tissue injury, the inflammatory process begins immediately, with pro-inflammatory M1 macrophages engulfing necrotic tissues and killing microbes during the inflammation phase. After the inflammation subsides, anti-inflammatory M2 macrophages release anti-inflammatory factors such as IL-10, TGF-β, and VEGF, promoting the progression from the inflammation to the proliferation phase [8]. However, high levels of reactive oxygen species (ROS) and inflammatory factors can hinder the phenotype transition between M1 and M2, leading to persistent inflammation and thus delaying the wound healing process [9,10]. Additionally, re-epithelialization, which begins in the proliferation phase, is a decisive factor for successful wound healing [11], but the oxidative stress environment can affect the viability and migration of keratinocytes, causing delays in re-epithelialization and granulation tissue formation [12]. Furthermore, fibroblasts are recruited to the wound site during the inflammatory phase, activated in a low-stress environment, then proliferate and secrete collagen, and the TGF-β1 profibrotic niche created by macrophages can induce and maintain the differentiation of fibroblasts into the highly contractile α-SMA-positive myofibroblasts, driving collagen hardening and mediating fibrotic repair, thus restoring the mechanical integrity of the skin [13–16]. However, the fibrotic repair can enhance the sustained activation of the highly contractile α-SMA-positive myofibroblasts, leading to further exacerbation of tissue fibrosis [15]. Meanwhile, the highly contractile α-SMA-positive myofibroblasts produce less collagen [14,15]. Therefore, breaking this positive feedback loop is one of the most challenging yet promising strategies for anti-fibrotic or pro-healing therapies targeting myofibroblasts. Hence, restoring the normal function of fibroblasts is crucial. Against this backdrop, various hydrogels with unique biological functions have been developed and utilized to promote wound healing through the introduction of bioactive molecules or drugs as dressings [17–19]. Despite significant progress, simultaneously regulating the inflammatory response, oxidative stress, and fibrotic repair remains a challenge.

Previous reports have indicated that mice overexpressing angiotensin-converting enzyme (ACE) in bone marrow-derived cells produce twice the amount of superoxide ($O_2^{\cdot-}$) by macrophages compared to wild-type (WT) mice, and treatment with the ACE inhibitor (ACEI) lisinopril can restore the WT phenotype [20,21]. Additionally, ACEI can inhibit the production of oxygen radicals by alveolar macrophages [22,23]. Simultaneously, ACE mediates the conversion of angiotensin I (Ang I) to Ang II, and Ang II can induce macrophage polarization into the pro-inflammatory M1 phenotype, increasing the expression of pro-inflammatory factors [24]. But in a study of non-small cell lung cancer development, ACEI has been shown to increase polarization towards the anti-inflammatory M2 macrophage phenotype [25]. Moreover, multiple studies have demonstrated the significant impact of ACE on various fibrotic diseases [26,27], including skin scarring [28,29]. Systemic application of ACEI can reverse the fibrotic process, such as improving myocardial remodeling after myocardial infarction [30], reducing the formation of skin scars [31,32]. Therefore, ACEI holds great potential for simultaneously regulating inflammatory response and fibrotic repair. Nevertheless, for patients without cardiovascular diseases, the long-term systemic use of ACEI to promote skin regeneration poses a risk of drug side effects, presenting challenges for the topical application of ACEI.

Traditional local drug delivery systems struggle to regulate the spatiotemporal release of drugs, and even encapsulating drugs within hydrogels can lead to rapid release rates due to material degradation, making it difficult to maintain local drug concentrations for extended periods. Furthermore, environmental factors such as temperature and oxidation can lead to the loss of drug active components. However, encapsulating drugs within biodegradable microspheres has become an indispensable part of new drug delivery systems [33]. Poly (lactic-co-glycolic acid) (PLGA), known for its good biocompatibility, degradability, and easy-to-process mechanical properties, has become a favored biomaterial for creating drug-encapsulated microspheres [34]. But applying drug microspheres only to lesion defects (such as skin wounds) still fails to achieve targeted local drug delivery. Without carriers like hydrogels, microspheres can easily be lost with bodily fluids or dislodge from the application site due to movement and friction, leading to rapid decreases in local drug concentration and reduced therapeutic effects. Moreover, hydrogels that mimic the natural extracellular matrix often exhibit swelling behavior, and the resulting volume expansion due to weakened cohesion can cause mechanical force dissipation and reduced adhesion [35,36]. Additionally, drug microspheres can easily escape from the physically expanded network structure [37], and the expansion stress can compress regenerating tissues [38]. Therefore, it is essential to develop a new type of non-swelling hydrogel dressing that can carry drug microspheres for long-term local application and provide multifunctional regulation of the microenvironment for wound skin regeneration.

Pluronic F-127 (PF127) is a thermosensitive triblock copolymer (PEO-PPO-PEO), which dissolves in water at low temperatures and forms a gel as the temperature rises. The thermosensitive hydrophobic segments (PPO) engage in multiple associative interactions, promoting self-assembly into ordered micro-regions and enhancing physical cross-linking. This dense physical cross-linking endows it with excellent self-shrinking capability and anti-swelling property, making it widely used in biosurfactants and drug delivery systems [38–40]. Additionally, gelatin, a hydrolyzed product of collagen, contains abundant RGD sequences that can bind to platelet integrin receptors, thus activating the coagulation cascade [41]. Gelatin's good biocompatibility, low antigenicity, and biodegradability make it an ideal precursor for forming cross-linked hydrogels [42,43]. Here, we used PLGA to load lisinopril to create lisinopril microspheres (LMs), whose slow-release properties enhance the stability of lisinopril release, prolong its duration, and increase local tissue cell absorption of the drug [44]. Simultaneously, to regulate the wound regeneration microenvironment and provide a carrier for drug microspheres, we designed and manufactured an active shrinkage and antioxidative hydrogel with biomimetic mechanics functions. This hydrogel was fluidic upon injection, adapting to irregular wound defects, and gradually solidified and shrank upon reaching body temperature. The reductive groups in the hydrogel enhanced tissue adhesiveness and mechanical stability, and imparted excellent antioxidative property. This versatile hydrogel (P&G) consisted of two interpenetrating polymer chains without any toxic cross-linker: 4-formylbenzoic acid-grafted PF127 (PF127-CHO) and carbonic dihydrazide (CDH)-modified gelatin (Gel-CDH), where the aldehyde groups on the PF127-CHO chains cross-linked with the amine groups on the Gel-CDH chains to form dynamic Schiff base bonds. Notably, embedding LMs into P&G to form P&G@LMs further enhanced the anti-swelling performance and adhesion of the hydrogel system, making it more closely mimic the mechanical behavior of the skin [45], and achieved the spatiotemporal release of drug microspheres, thus maintaining local drug concentrations and reducing the need for repeated administration in the microenvironment. The synthesized P&G@LMs promoted wound contraction at physiological body temperature, regulated inflammatory responses and oxidative stress levels in the microenvironment, and the sustained release of LMs could, to some extent, inhibit the excessive proliferation of fibroblasts and their differentiation into the highly contractile α-SMA-positive myofibroblasts. The self-shrinkage functionality of the hydrogel mimicked the contraction characteristic of myofibroblasts, and the skin-like elastic modulus could accommodate the skin dynamic changes and restore the mechanical integrity of wound defect, thereby partially substituting the mechanical role of myofibroblasts in fibrotic tissue repair and promoting skin regeneration (Fig. 1).

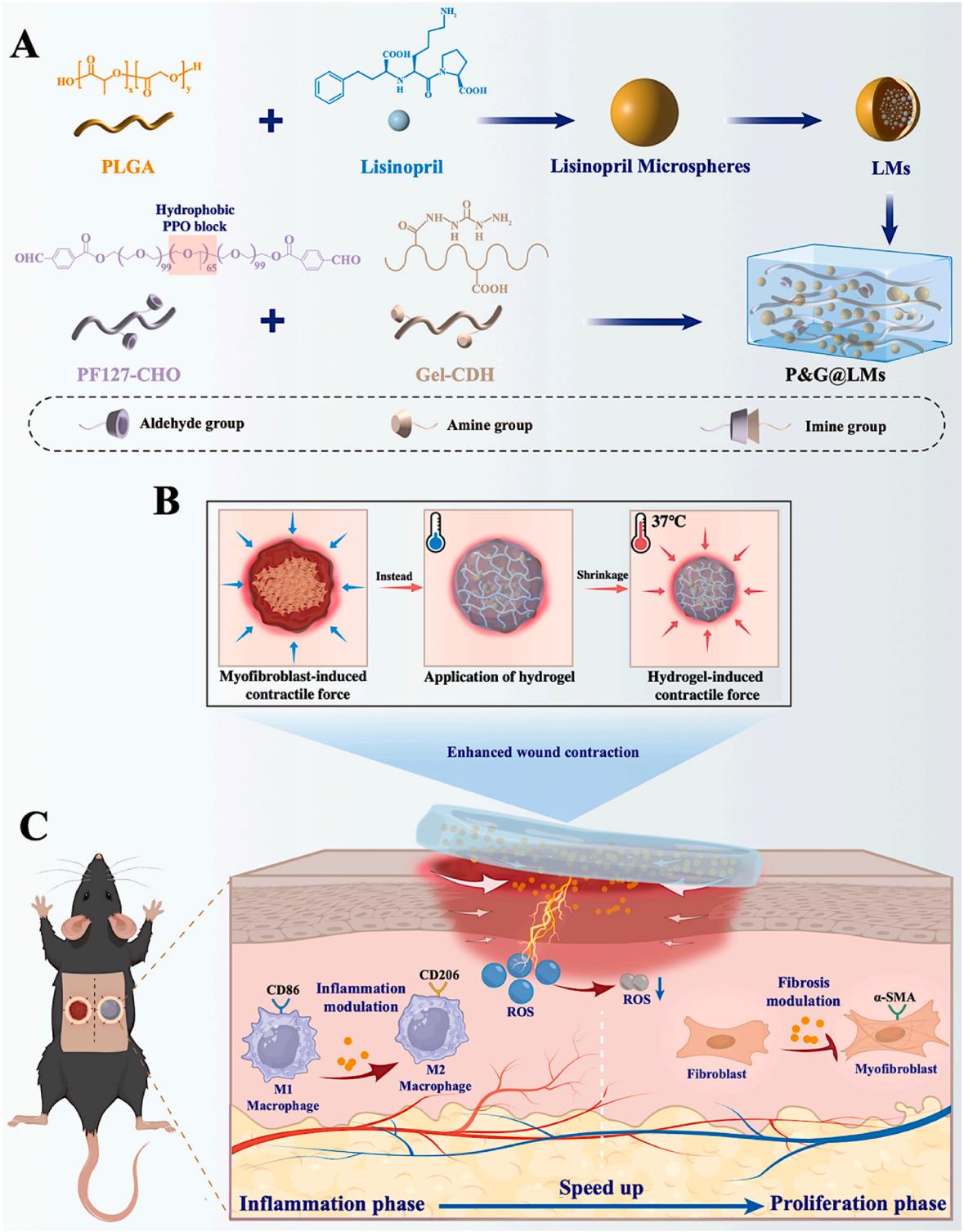

Fig. 1. An active shrinkage and antioxidative hydrogel with biomimetic mechanics functions modulates inflammation and fibrosis to promote skin regeneration. A) Preparation PF127-CHO/Gel-CDH (P&G) hydrogel loaded with LMs (P&G@LMs). B) P&G@LMs can replace partial contractile function of myofibroblast at the physiological temperature. C) Application of P&G@LMs on the mouse full-thickness wound excision silicone splint model to promote skin regeneration via scavenging ROS and modulating inflammation and fibrosis.

2. Results and discussion

2.1. Preparation and characterization of PF127-CHO, Gel-CDH and P&G hydrogel

Due to the greater stability of aromatic Schiff base bonds compared to aliphatic ones [46], we opted to graft 4-formylbenzoic acid onto PF127 to yield the benzaldehyde-terminated PF127 (PF127-CHO) [47]. Subsequently, Gel-CDH was synthesized via amidation reaction between the carboxyl groups on gelatin and the amine groups on carbonic dihydrazide (CDH) (Figure S1, Supporting Information) [48]. Without the addition of any toxic crosslinking agents, the hydrogel was then

prepared by mixing PF127-CHO with Gel-CDH at room temperature (25 °C) using an in situ crosslinking method, forming dynamic Schiff base bonds through the aldehyde groups and amine groups as cross-linking points (Fig. 2A). Fourier-transform infrared (FTIR) spectroscopy was used to analyze the chemical structure of the polymers. As shown in Fig. 2B and Figure S2 (Supporting Information), a strong absorption peak appeared at 1710 cm^{-1}, which was a typical C=O stretching of benzaldehyde [49]. The modification of gelatin was reflected in heightened peaks of Gel-CDH at 1240 (amide III), 1543 (amide II), 1655 (amide I), and 3322 cm^{-1} (amide A) [48]. The spectrum of PF127-CHO/Gel-CDH (P&G) showed a new intense absorption peak of the imine structure (C=N) at 1647 cm^{-1}, with the disappearance of C=O stretching of the aldehyde group, indicative of a Schiff base reaction between the amine groups in Gel-CDH and the aldehyde groups in PF127-CHO [50].

2.2. Preparation and characterization of lisinopril microspheres (LMs)

LMs were prepared following a previously reported method [51], as outlined in Fig. 2C. The microstructure of LMs was further characterized by scanning electron microscopy (SEM) (Fig. 2D). After homogenization, the surface of LMs appeared relatively smooth without evident cracks, with particle size distribution concentrated within the range of 0.5–1.5 μm (Fig. 2E). This size range is smaller than the average diameter of most cells, allowing the microspheres to fully contact and exert their effects on the cells. Moreover, the maximum absorption peak of lisinopril was determined to be at 210 nm using UV–Vis spectrophotometry (Fig. 2F), and the standard curve of lisinopril was generated through linear regression analysis (Fig. 2G). Subsequently, based on the standard curve, the drug loading rate and encapsulation rate of LMs were calculated to be 4.5 ± 0.6 % and 45 ± 6 %, respectively.

2.3. Composition design and characterization of P&G and P&G@LMs

2.3.1. Composition design of P&G and P&G@LMs

25 % w/v PF127-CHO and 8 % w/v Gel-CDH were mixed at room temperature in volume ratios of 1:2, 1:3, and 1:4 to form P&G2, P&G3, and P&G4, respectively. Then, LMs were embedded into the P&G hydrogel to form P&G2@LMs, P&G3@LMs, and P&G4@LMs. The microstructure of the hydrogel was observed using SEM (Fig. 2I), revealing that the P&G2 hydrogel had larger and more regular pores with thicker pore walls compared to the other two groups. However, as the proportion of Gel-CDH increased, the pore size in the hydrogels decreased, the pore walls became thinner, and the structure became disordered and even collapsed, which might be due to insufficient cross-linking. Furthermore, the embedding of LMs had no discernible impact on the cross-linking of the hydrogel.

Swelling is a critical issue when hydrogel contacts with hydrated tissue interfaces, as water molecules permeate the hydrophilic hydrogel network, thereby reducing the mechanical property of the hydrogel [36,38]. After fully immersing hydrogels in PBS, the swelling behavior was depicted in Fig. 2H and Fig. S3 (Supporting Information). Only the P&G4 hydrogel showed obvious swelling after 24 h, with a swelling ratio greater than 10 %, while the other groups showed no significant changes, possibly due to the higher proportion of Gel-CDH (Gelatin has a strong water-absorbing capacity, approximately 5–10 times its own weight). This indicated that the P&G hydrogel possessed excellent anti-swelling property, and all P&G@LMs also exhibited similar anti-swelling behaviors (Fig. 2J). The PLGA used to make LMs is produced by the polymerization reaction between PLA and PGA. The methyl side groups in PLA contribute to its increased hydrophobicity compared to PGA, leading to the lactide-rich PLGA copolymer being less hydrophilic. As a result, the copolymer absorbs less water and degrades at a slower rate [52]. Hence, when the relatively hydrophobic LMs were embedded into the hydrophobic P&G to form P&G@LMs, they increased the overall hydrophobicity of the hydrogel to some extent. Current study has reported these findings similar to our results [53]. Interestingly, the anti-swelling characteristic also conferred advantages for the application of the hydrogel. When P&G and P&G@LMs are applied to wound defects, they will not exert excessive stress on the surrounding tissues due to swelling.

The degradation rates of hydrogels were then assessed (Fig. 2K and Fig. S4, Supporting Information). P&G3 and P&G4 hydrogels degraded completely within 4 days, while P&G2 hydrogel lasted until day 8. All P&G@LMs showed significantly slower degradation rates, presumably due to the increased hydrophobicity caused by the PLGA used to make the LMs. Embedding the relatively hydrophobic LMs into the hydrogels increased the materials' overall hydrophobicity to some extent and slowed down the rate at which water molecules penetrated the hydrogels, potentially extending their degradation time [53]. Nonetheless, this degradation timeline is advantageous for wound tissue repair, as prolonged degradation may exert undue pressure on newly granulation tissue and blood vessels, whereas excessively rapid degradation can curtail the therapeutic duration of the drug's efficacy. And when the hydrogel adhered to the wound site, it remained relatively stationary with respect to the wound. To clearly demonstrate the release process of LMs from P&G@LMs, 300 μL of P&G@LMs adhered to the bottom of the 6-well plate, with 2 mL of PBS added to each well, and the plate was placed in a 37 °C environment. We made every effort to avoid liquid agitation when moving the plate and taking photographs, so there might be aggregation and deposition of the degradation products from the hydrogel and microspheres. The images clearly demonstrated that the degradation process unfolded in a layered manner from the exterior to the interior, rather than by swelling-induced rupture of the mesh walls (Fig. 2M and Fig. S5, Supporting Information). Fig. 2N illustrated that the controlled release of LMs was facilitated by the methodical degradation of the P&G@LMs network.

Additionally, LMs, P&G2@Lis, and P&G2@LMs (each containing an equal amount of lisinopril) were immersed in PBS to assess the drug release. Fig. 2L showed the in vitro release curves of lisinopril, indicating rapid drug release from LMs, with a release rate exceeding 90 % within three days. When encapsulated within P&G2 hydrogel, despite the hydrogel slowing down the drug release, the release rate still surpassed 90 % after eight days. Notably, in P&G2@LMs, the drug was released totally after the degradation of both the hydrogel and the microspheres, reaching a release rate of about 70 % after eight days, which further highlighted the sustained release capability of the P&G@LMs system for lisinopril. Concurrently, the repair of skin wound, encompassing both the formation of granulation tissue and re-epithelialization, advances from the periphery to the center of the wound [54,55]. This spatial and temporal alignment with the layer-by-layer degradation and phased release of P&G@LMs ensured that the gradual delivery of the drug accurately corresponded to the specific requirements of different phases of skin wound healing, thereby enhancing therapeutic efficacy.

2.3.2. Mechanical properties of P&G and P&G@LMs

Skin possesses inherent elasticity and mechanical strength, making the design of biomimetic hydrogels that emulate skin mechanics significant for biomaterial applications, these can be assessed through rheology and elasticity testing. As shown in Fig. 3A, P&G hydrogels could withstand a certain degree of stretching and compression. Frequency sweep results indicated that the storage moduli (G') of the hydrogels were significantly higher than their loss moduli (G'') when the frequency increased from 0.1 Hz to 10 Hz, revealing the long-term structural stability of the P&G and P&G@LMs as elastomers (Fig. 3B and D). Additionally, the average G' of all hydrogels at 1 Hz and 37 °C was assessed, with P&G2 and P&G2@LMs showing the highest average G' (Fig. 3C and E). Tensile strain testing results indicated that the tensile moduli of P&G and P&G@LMs ranged from 24.13 kPa to 41 kPa and from 33.13 kPa to 43.97 kPa, respectively (Fig. 3F–I). Compression strain testing results showed that the compression moduli of P&G and P&G@LMs ranged from 12.4 kPa to 16.17 kPa and from 12.57 kPa to

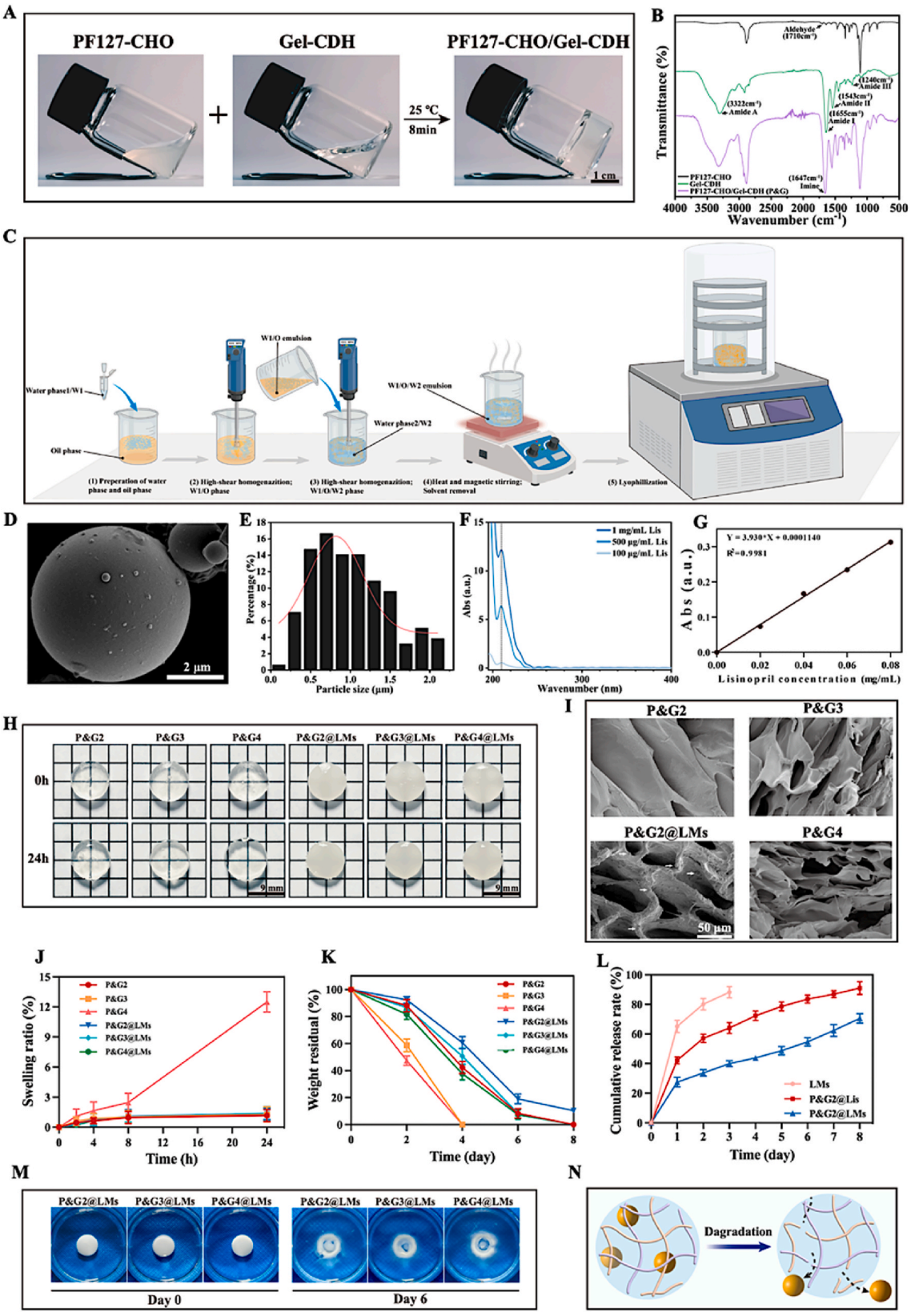

Fig. 2. Preparation and characterization of P&G, LMs, and P&G@LMs. A) Macroscopically illustration of gelation of PF127-CHO and Gel-CDH (scale bar = 1 cm). B) FTIR spectra of PF127-CHO, Gel-CDH, and P&G hydrogel. C) Schematic showing the preparation of lisinopril microspheres (LMs). D) Representative SEM image of LMs (scale bar = 2 μm). G) Size distribution of LMs. F) UV–Vis spectrum of lisinopril. G) Standard curve for lisinopril. H) 24h swelling images of P&G and P&G@LMs (scale bar = 9 mm). I) Representative SEM images of P&G and P&G@LMs (scale bar = 50 μm). White arrow: microspheres. J) 24h swelling rates of P&G and P&G@LMs (n = 3). K) Degradation rates of P&G and P&G@LMs (n = 3). L) Cumulative release of lisinopril from LMs, P&G2@Lis, and P&G2@LMs (n = 3). M) P&G@LMs released LMs in a layered manner from the exterior to the interior. N) Schematic showing the LMs release from hydrogel degradation. Error bars represent the mean ± standard deviation.

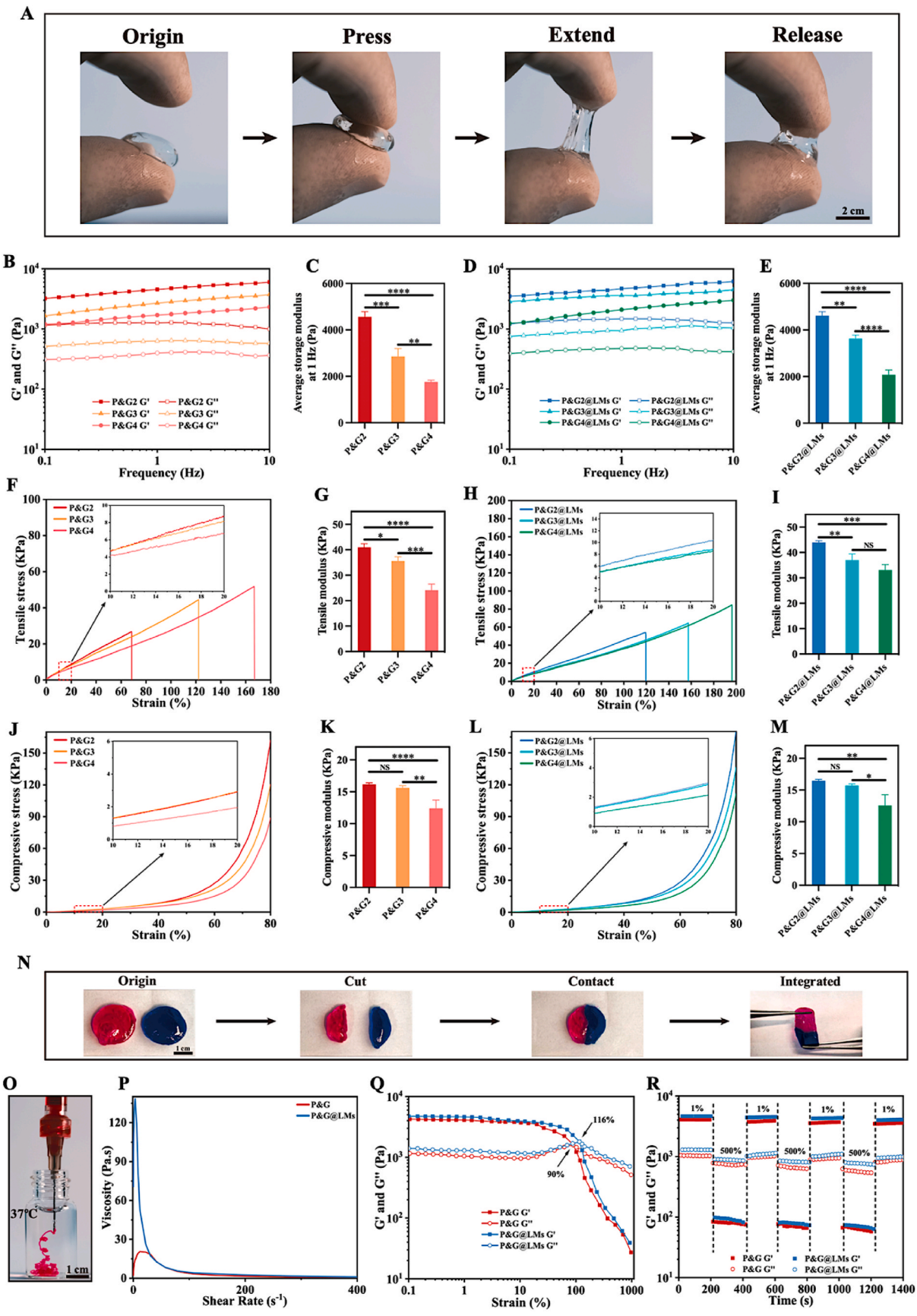

(caption on next page)

Fig. 3. Characterization the mechanical property of P&G and P&G@LMs. A) Images showing the compressible and tensible nature of the hydrogel (scale bar = 2 cm). B) and D) Frequency sweep tests (from 0.1 to 10 Hz) of P&G and P&G@LMs at 37 °C. C) and E) Quantitative analysis of average storage moduli at 1 Hz of P&G and P&G@LMs determined by frequency sweep tests (n = 3). F) and H) Tensile stress-strain curves of P&G and P&G@LMs. G) and I) Tensile moduli of P&G and P&G@LMs in the 10–20 % strain range of the tensile curves (n = 3). J) and L) Compression stress-strain curves of P&G and P&G@LMs. K) and M) Compression moduli of P&G and P&G@LMs in the 10–20 % strain range of the compression curves (n = 3). N) Macroscopically illustration of the self-healing process of P&G dyed with rhodamine B and methylene blue (scale bar = 1 cm). O) Image of P&G injected through a 26-G needle into 37 °C PBS (scale bar = 1 cm). P) Viscosity measurements of P&G and P&G@LMs with increasing shear rate (0.1–1000 s^{-1}) at a fixed frequency of 1 Hz at 37 °C. Q) Rheological property of P&G and P&G@LMs in the strain amplitude sweep (γ = 0.1–1000 %) at 1 Hz and 37 °C. R) Rheological property of P&G and P&G@LMs at low (1 %) and high (500 %) strains with loading time of 200s, respectively. Error bars represent the mean ± standard deviation. *P < 0.05; **P < 0.01; ***P < 0.001; ****P < 0.0001; NS, not statistically significant.

16.47 kPa, respectively (Fig. 3J–M). The rheological and elasticity testing results were consistent, indicating that the increased crosslinking density in P&G2 and P&G2@LMs enhanced mechanical strength, providing robustness. Ideally, the elastic modulus of hydrogel dressing should match the modulus of underlying and adjacent tissues to ensure structural integrity and accommodate tissue dynamics. In this study, the elastic moduli of all P&G and P&G@LMs hydrogels were comparable to human skin (5 kPa–140 MPa) [45]. Comprehensively considering the mechanical, anti-swelling, and degradation behaviors, P&G2 and P&G2@LMs hydrogels were selected for subsequent experiments due to their excellent properties.

It is noteworthy that the injectability and self-healing property of hydrogel provide unique advantages for localized treatment. Injectability allows the hydrogel to fill irregular wound surfaces, and self-healing enables the hydrogel to repair itself after mechanical damage, thus extending its lifespan. Rhodamine B-dyed P&G hydrogels could be continuously injected into 37 °C PBS through a 26-G needle without clogging (Fig. 3O). The shear viscosity curves indicated that as the temperature of the rheometer's plate was heated to 37 °C, the viscosities of both hydrogels suddenly increased (Fig. 3P). This phenomenon arises from the intensified aggregation of the hydrophobic PPO segments with rising temperature, which accelerates the gelation speed and increases the viscosity [40,56]. The addition of LMs significantly increased the viscosity of the P&G@LMs, as increasing the solid content in the hydrogel tends to enhance the hydrogel's viscosity [57]. However, as the shear rate increased, the viscosity of the hydrogels rapidly decreased, demonstrating the typical shear-thinning behaviors of P&G and P&G@LMs [58]. Fig. 3N showed the macroscopic self-healing of the hydrogel. The strain amplitude scan test was first used to determine the critical strain point of the hydrogels. As shown in Fig. 3Q, P&G and P&G@LMs intersected at strains of 90 % and 116 %, respectively. When a strain greater than the critical point was applied, G″ became less than G′, indicating the collapse of the hydrogel network. Subsequently, a continuous alternating strain test was conducted to evaluate the self-healing properties of the hydrogels (Fig. 3R). At higher strains (500 %), the network structure of the hydrogels was completely destroyed, but upon reducing the strain to 1 %, the crosslinked network effectively recovered. The results of the continuous alternating strain tests showed that the collapse and recovery of the hydrogel network were reversible, and could be maintained across multiple repeated cycles, indicating their efficient self-healing capabilities [58].

2.3.3. Adhesion, contraction, hemostasis, water-retention, and biocompatibility of P&G and P&G@LMs

Good tissue adhesion capacity is crucial for wound dressings, as chemically modified hydrogels can adhere firmly to tissue surfaces through covalent bonds. Additionally, anti-swelling property allows hydrogel to minimize mechanical force dissipation and adapt to the dynamic changes of tissues [36,38], enabling the slow spatiotemporal release of drugs. Moreover, the hydrogel will contract when the outward expansion force is less than the temperature-responsive inward contraction force. Fig. 4A and Fig. S6 (Supporting Information) demonstrated the macroscopic adhesion of P&G hydrogel, which remained intact and tightly adhered to tissue after bending, twisting, and pulling, indicating that the hydrogel could accommodate the dynamic changes of the skin. In addition, we verified the stable adhesive property of the hydrogels in a moist environment. We applied the hydrogels to the fresh porcine skin and placed it in a 37 °C environment for 30 min. Subsequently, after soaking in PBS for 24 h or rinsing with running water, the hydrogel remained intact and tightly adhered to the porcine skin (Fig. S7 and Video S1, Supporting Information). Subsequently, lap shear tests were conducted using fresh porcine skin to quantify the tissue adhesion strength of P&G and P&G@LMs (Fig. 4B). As shown in Fig. 4C and D, their adhesion strengths were 15.05 ± 3.87 kPa and 33.27 ± 7.03 kPa, respectively, indicating good adhesive properties of the hydrogels. Gel-CDH in the synthesized P&G hydrogel contained numerous carboxyl and amino groups that could form hydrogen bonds with the amino and carboxyl groups on skin tissues. Additionally, the PLGA used in synthesizing LMs, contained a large number of hydroxyl and carboxyl groups, thereby forming additional hydrogen bonds with the amino and carboxyl groups on the skin. This likely explained why the inclusion of LMs enhanced the tissue adhesion of the hydrogel. Fig. 4E illustrated P&G@LMs formed new Schiff base bonds or hydrogen bonds with the carboxyl or amino groups of peptides or proteins on skin tissues, thereby enhancing adhesion strength. More importantly, the formed hydrogels exhibited asymmetric adhesion. We applied the hydrogels to the fresh porcine skin and placed it in a 37 °C environment. After 30 min, when covered with a normal dressing, the hydrogels did not adhere to the dressing, suggesting that removing the dressing would not cause the hydrogels to tear off from the skin, thereby preventing tissue damage (Fig. 4F and Video S2, Supporting Information).

Wound healing progresses from the periphery towards the center [54,55], a temperature-responsive contractile hydrogel can promote wound contraction and accelerate the healing process. Fig. 4G and H demonstrated the self-contraction capability of P&G and P&G@LMs at 37 °C after 1 h, with both exhibiting approximately 20 % self-contraction. Fig. 4I showed the self-contraction mechanism of the hydrogel as the temperature rose: the hydrophobic domains (PPO segments in PF127-CHO) gradually aggregated due to the increased temperature [40,56]. These hydrophobic segments, through multipoint associative interactions, drive the molecular chains to self-assemble into ordered micro-regions, thereby strengthening physical cross-linking. This dense physical cross-linking grants the hydrogel exceptional anti-swelling property and self-contraction ability [59]. When the expansive force within the polymer network of the hydrogel is less than its contractive force, the hydrogel's volume will contract [38]. Fig. 4J provided a schematic showing that the hydrogel induced wound contraction at the physiological temperature.

Hemostasis marks the initial phase of wound healing [2]. An ideal wound dressing should promptly activate coagulation signals and facilitate rapid clot formation without necessitating additional pressure. Injectable hydrogel offers considerable advantages for hemostatic wound dressing applications. Irregular filling and adhesion maximize the contact area between the hydrogel and the wound site, thereby achieving effective hemostasis. For this purpose, a liver hemorrhage model was established to evaluate the hemostatic ability of the hydrogel. As shown in Fig. 4K, L, and S8 (Supporting Information), the untreated group bled 341.5 ± 30.5 mg within 60 s, while the hydrogel-treated group bled only 114.3 ± 16.4 mg. Due to the abundant RGD sequences on gelatin, which can recognize and activate coagulation signals via cellular integrin receptors [41], and the formation of both

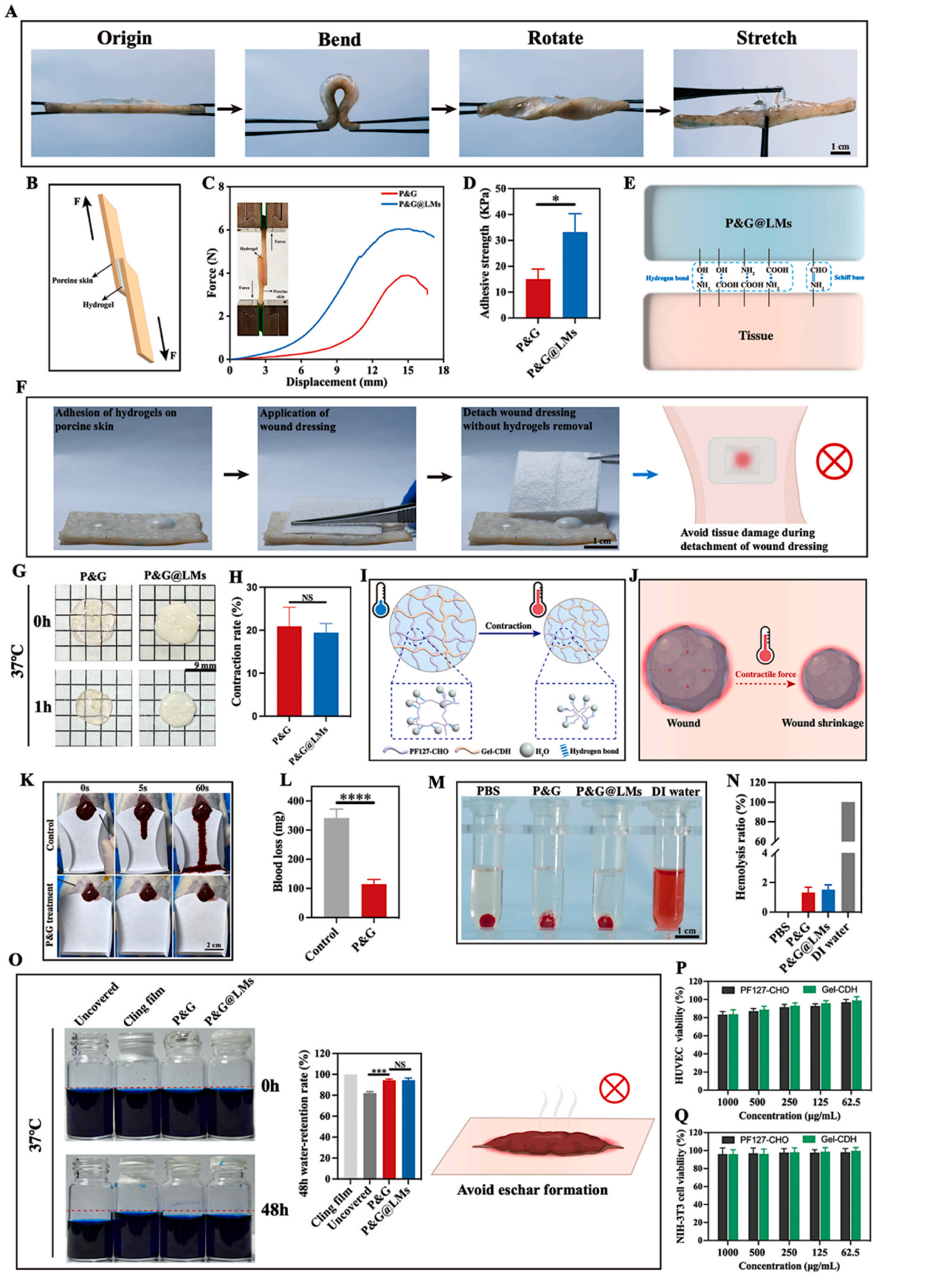

(caption on next page)

Fig. 4. Adhesion, contraction, hemostasis, water-retention, and biocompatibility of P&G and P&G@LMs. A) Macroscopically illustration of adhesion of P&G on porcine skin (scale bar = 1 cm). B) Schematic diagram of the lap shear test using porcine skin. C) Typical force-displacement curves of porcine skin bonded to P&G and P&G@LMs. D) Quantitative analysis of adhesive strength of P&G and P&G@LMs calculated from the force-displacement curves (n = 3). E) Schematic illustration of adhesive performance of P&G@LMs with the skin tissue surface. F) The hydrogels exhibited asymmetric adhesion after gelation on porcine skin (scale bar = 1 cm). G) The active contraction of P&G and P&G@LMs placed in 37 °C environment after 1 h (scale bar = 9 mm). H) Quantitative analysis of contraction properties (n = 3). I) Schematic illustration of the contraction mechanism of P&G and P&G@LMs at body temperature. J) Schematic illustration of the wound shrinkage by P&G and P&G@LMs at body temperature. K) Images of application of the hydrogel to the liver hemostasis (scale bar = 2 cm). L) Quantitative analysis of blood loss (n = 3). M) Hemocompatibility of P&G and P&G@LMs (scale bar = 1 cm). N) Quantitative results of the hemolytic test (n = 3). O)The hydrogels could create a relatively sealed environment to reduce water loss and thereby potentially prevented eschar formation. P-Q) Cell viability for both NIH-3T3 and HUVEC exposed to precursor solutions at various concentrations. Error bars represent the mean ± standard deviation. *P < 0.05; **P < 0.01; ***P < 0.001; ****P < 0.0001; NS, not statistically significant.

covalent and non-covalent bonds between the hydrogel and tissue, a hemostatic protective barrier was established.

Simultaneously, possessing excellent blood compatibility is vital for hydrogel wound dressings. The blood compatibility of the hydrogel was evaluated by hemolysis test. Phosphate buffered saline (PBS) and deionized (DI) water were used as negative control (no hemolysis) and positive control (obvious hemolysis), respectively. Fig. 4M showed photographs of the centrifuged samples, where the supernatants in all groups were clear except the DI water group, indicating no significant destruction of red blood cells and no release of hemoglobin. With the DI water group representing 100 % hemolysis, the hemolysis percentages for P&G and P&G@LMs were both lower than 2 % (Fig. 4N). A hemolysis rate below 5 % is considered to demonstrate good biocompatibility for polymeric materials [60]. Thus, it was evident that P&G and P&G@LMs exhibited excellent blood compatibility and could be safely applied to wounds without causing hemolytic reactions.

At the same time, a moist environment is conducive to wound healing and tissue regeneration [61]. Currently, most hydrogels maintain a moist wound healing environment in two ways: either through their own high-water content or by absorbing wound exudate [62]. However, the expansion of hydrogel volume inevitably compresses the regenerated tissue [38]. In this study, the designed anti-swelling hydrogel could seal the wound, and the exudate underneath could provide a moist environment for wound healing. The water evaporation method was employed to simulate and verify the hydrogels' ability to maintain moisture after sealing the wound. As shown in Fig. 4O and Fig. S9 (Supporting Information), after 48 h, compared to the cling film group with a 100 % water retention rate, both P&G and P&G@LMs had a water retention rate of approximately 94.4 %, while the unsealed group had a rate of about 82.2 %. This suggested that the hydrogels could prevent the loss of exudate to some extent after covering the wound, thereby providing a moist environment for wound healing and potentially preventing eschar formation.

Additionally, favorable biocompatibility of the hydrogel polymer precursor solution is a fundamental requirement for biomedical applications. The hydrogel precursor solution was co-cultured with human umbilical vein endothelial cells (HUVEC) and fibroblasts (NIH-3T3) at concentrations of 0.0625–1 mg/mL for 24 h, and the MTT assay was used to detect cell viability to evaluate the cell compatibility of the hydrogel precursor solution. Our findings indicated that viability for both cell types exposed to precursor solutions at various concentrations exceeded 80 % (Fig. 4N and O), this indicated that the hydrogel had good cytocompatibility. According to the ISO 10993-5 international standard, a cell survival rate of over 80 % is considered non-cytotoxic [63].

2.4. Antioxidant and anti-inflammatory capacities of P&G and P&G@LMs in vitro

In the inflammation phase of wound healing, macrophages play a crucial role in maintaining microenvironmental homeostasis by regulating ROS secretion [64]. Low levels of ROS can preserve normal cellular functions and microenvironmental balance, including stimulating angiogenesis through vascular endothelial growth factor (VEGF) signaling and promoting the migration and proliferation of keratinocytes [65]. However, high levels of ROS can lead to persistent secretion of pro-inflammatory cytokines and induce cell death by activating apoptotic proteins [66,67]. Biomaterials with specific functions should have the capability to modulate macrophage polarization and regulate the oxidative stress microenvironment.

The antioxidant potential of the hydrogels was initially evaluated using DPPH and NBT free radical scavenging assays. As depicted in Fig. 5A and C, introducing the hydrogels resulted in a noticeable lightning of the solution laden with free radicals. Compared to the control group, both demonstrated an ability to neutralize over 40 % of free radicals (Fig. 5B and D), suggesting that P&G and P&G@LMs exhibited substantial antioxidant capabilities, capable of modulating oxidative stress within the wound healing microenvironment. Additionally, LMs did not have the ROS scavenging ability, and the addition of LMs to the hydrogel would not affect the removal of ROS by P&G@LMs. This efficacy was likely attributable to the hydrogels' rich content of reductive amino acid sequences and hydrazide groups, which actively scavenge free radicals. Meanwhile, the antioxidant capability could also preserve the bioactivity of the encapsulated drugs to a significant extent.

Moreover, to further evaluate the hydrogels' capability to mitigate intracellular ROS following oxidative stress damage during the inflammation phase, we developed a hydrogen peroxide (H_2O_2)-induced macrophage (RAW 264.7) oxidative damage model and assessed using DCFH-DA fluorescent staining and flow cytometry (FCM). As shown in Fig. 5E, RAW264.7 cells exposed to H_2O_2 exhibited strong DCF fluorescence intensity, confirming the existence of intracellular ROS [68]. However, subsequent co-culturing with P&G and P&G@LMs resulted in a reduction of fluorescence intensity to levels comparable to those of the control group (Fig. 5F and G), with the inclusion of LMs having no detrimental effect on this outcome. Furthermore, cell viability was assessed using the MTT assay. Compared to the H_2O_2 group, the cell survival rates in the hydrogel groups significantly increased, reaching over 80 % (Fig. 5H). This underscored that the hydrogels could enhance the macrophages' ability to resist oxidative stress by scavenging exogenous oxidants, thereby ensuring cell survival. In addition, as shown in Fig. 5I and L, the ROS levels increased after the stimulation with LPS, but the application of hydrogels significantly decreased ROS produced by macrophages. This suggested that P&G@LMs could have the potential to modulate the inflammatory microenvironment as well.

Most critically, macrophages can become imbalanced between the pro-inflammatory M1 phenotype (expressing CD86) and the anti-inflammatory M2 phenotype (expressing CD206) under inflammatory stimuli. This imbalance leads to increased ROS production and sustained inflammation in the microenvironment, thereby delaying the wound healing process [9]. To address this, we further evaluated the impact of P&G and P&G@LMs on macrophage polarization, using lipopolysaccharide (LPS)-induced M1 phenotype as a positive control and interleukin-4 (IL-4)-induced M2 phenotype as a negative control. Immunofluorescence staining was employed to ascertain the macrophage polarization state, enabling visualization of CD86 and CD206 expression triggered by LPS and IL-4, respectively. Diminished CD86 expression coupled with elevated CD206 levels were observed in the P&G@LMs group compared to the LPS group (positive control),

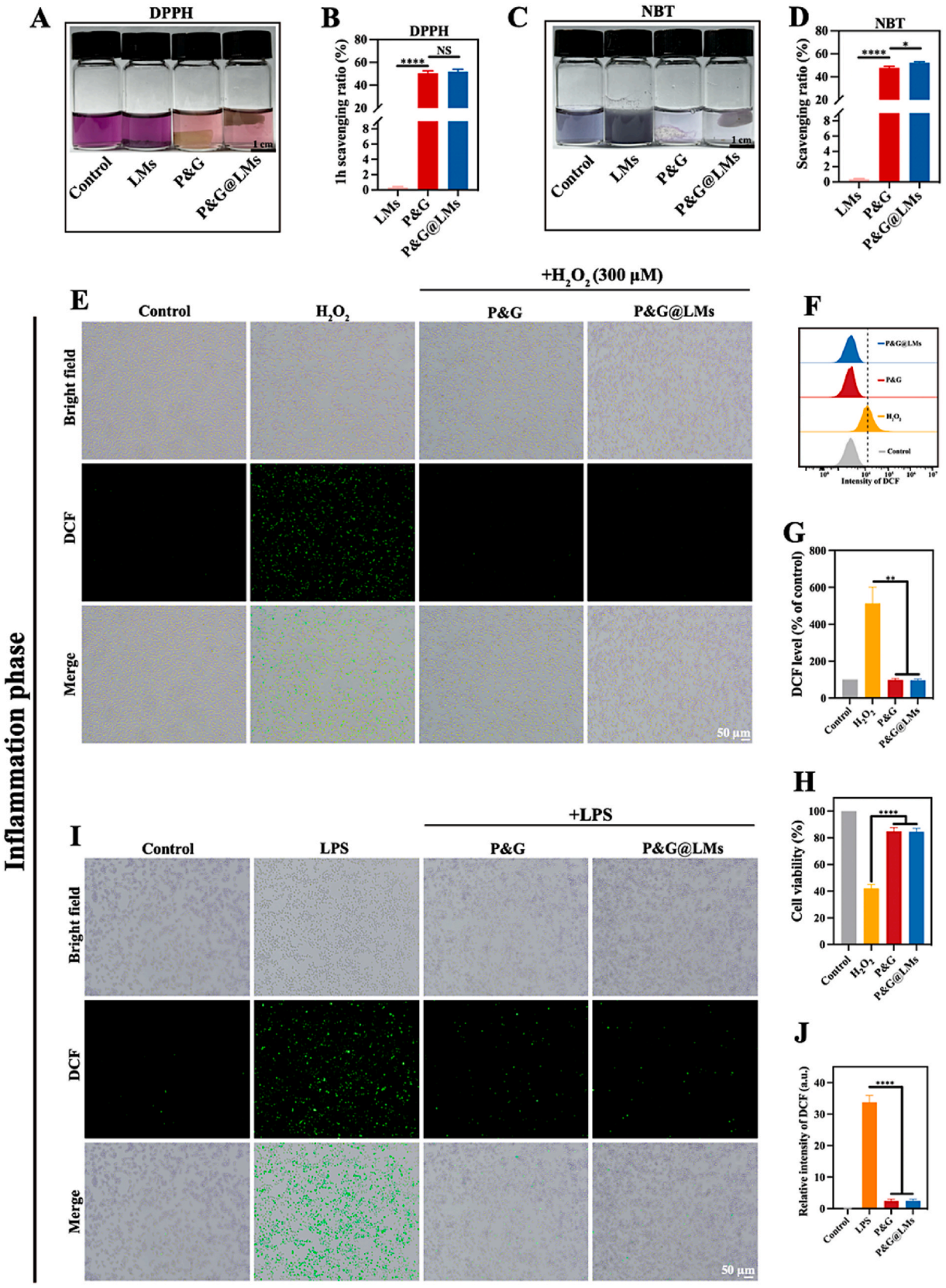

Fig. 5. Antioxidant capacity of P&G and P&G@LMs in vitro. A) and C) Images of DPPH and NBT free radicals scavenging of P&G and P&G@LMs for 1 h (scale bar = 1 cm). B) and D) Quantitative results of the scavenging property (n = 3). E) ROS-scavenging effect of P&G and P&G@LMs on RAW264.7 cells detected by fluorescence microscope (scale bar = 50 μm). F) ROS levels detected by FCM. G) Quantitative analysis of ROS levels according to FCM (n = 3). H) Survival percentages of RAW 264.7 cells when subjected to P&G and P&G@LMs in a H_2O_2-rich medium (300 μM). I) ROS levels of RAW 264.7 cells treated with LPS, P&G, and P&G@LMs and detected by fluorescence microscope (scale bar = 50 μm). J) Statistical histogram of relative ROS levels (n = 3). Error bars represent the mean ± standard deviation. *P < 0.05; **P < 0.01; ***P < 0.001; ****P < 0.0001; NS, not statistically significant.

indicating a shift toward M2 macrophage activation (Fig. 6A, C, and 6D). These trends were further confirmed by flow cytometry (FCM) data (Fig. 6B). In the group receiving P&G@LMs treatment, there was a decrease in the percentage of M1-like macrophages (CD86+CD206-) and an increase in M2-like macrophages (CD206+CD86-), as shown in Fig. 6E and F. Additionally, mRNA quantification via quantitative polymerase chain reaction (q-PCR) aligned with the immunofluorescence staining results and the FCM results, confirming the observed trends. The mRNA levels of IL-6, iNOS, Arg-1, and TGF-β1 were evaluated respectively (Fig. 6G–J), compared with the positive control group, the mRNA expression of the inflammatory markers IL-6 and iNOS reduced significantly, whereas the mRNA expression of the anti-inflammatory markers Arg-1 and TGF-β1 elevated in the cells treated with P&G@LMs. These findings suggested that P&G@LMs could regulate the inflammatory microenvironment.

2.5. Regulation of cellular migration, proliferation, and differentiation by P&G and P&G@LMs in vitro

In the proliferation and remodeling phases of wound healing, the migration capacity of keratinocytes determines the extent of re-epithelialization and is also pivotal for the success or failure of wound healing. However, high levels of ROS can lead to increased apoptosis and impaired migration of keratinocytes, thereby delaying re-epithelialization [66,67]. To address this, we utilized HaCaT cells to establish a cellular wound healing model, evaluating the impact of P&G and P&G@LMs on cell migration under oxidative stress conditions through scratch assays. As depicted in Fig. 7A, cell migration decreased after treatment with 100 μM H_2O_2 for 24 h, and by 48 h, the migration was significantly inhibited. Nonetheless, this inhibition was substantially mitigated in the hydrogel groups (Fig. 7B and C). These results suggested that the hydrogels were capable of facilitating cell migration even in the condition of high oxidative stress, and that the inclusion of LMs did not impede this process. This underscored the hydrogels' potential to promote wound healing.

Additionally, we assessed the biocompatibility of the hydrogels and investigated the impact of gradually released LMs (ACEI) on the proliferation and differentiation of mouse fibroblasts (NIH-3T3) through direct co-culturing with P&G@LMs (Fig. 7D). Cell proliferation was evaluated using the live/dead staining and the MTT assay. As shown in Fig. 7E and F, after 3 and 5 days of co-culture with P&G hydrogel, there was no significant impact on cell proliferation nor any notable cell death compared to the control group, indicating good biocompatibility of both the hydrogel precursor solution (Fig. 4P and Q) and the synthesized hydrogel. Conversely, fibroblast proliferation was reduced by over 42 % after 3 and 5 days of co-culture with P&G@LMs compared to the P&G group, indicating that the slow release of ACEI from P&G@LMs effectively inhibited fibroblast proliferation, as previous studies have reported that ACEI can inhibit fibroblasts proliferation [31,69]. And we used immunofluorescence to analyze the effects of P&G and P&G@LMs on the differentiation of fibroblasts into the highly contractile α-SMA--positive myofibroblasts. As shown in Fig. 7G and H, under TGF-β1 stimulation, there was a clear increase in the differentiation of fibroblasts into the highly contractile α-SMA-positive myofibroblasts, as evidenced by the elevated α-SMA expression [14], while P&G did not influence this process. But co-culturing with P&G@LMs significantly inhibited the differentiation into myofibroblasts due to the effect of LMs (ACEI). These results suggested that the controlled release of ACEI from P&G@LMs could substantially modulate fibroblasts proliferation and differentiation, thereby exhibiting a pronounced anti-fibrotic effect [31, 69]. And Fig. 7I showed the regulatory effects of LMs (ACEI) on macrophages and fibroblasts.

2.6. Therapeutic effects of P&G and P&G@LMs on skin regeneration

Inspired by the aforementioned results, we established a full-thickness excisional wound splinting model in C57BL/6 mice (Φ: 8 mm) to evaluate the effects of P&G and P&G@LMs on skin regeneration. The model involved excising the full thickness of the dorsal skin and subcutaneous fascia of the mice, tightly adhering and suturing a silicone ring around the periphery of the wound. And the model has proven to be prone to be a fibrosis-prone model [70–72]. This method prevents contraction-driven healing, which is typical in mice, and instead promotes healing through granulation tissue formation and re-epithelialization, closely mimicking the human wound healing process [73]. Fig. 8A illustrated the mouse dorsal silicone ring model, hydrogel application, and sample collection. The mice were randomly divided into four groups: control, P&G, LMs, and P&G@LMs (Fig. 8B), with macroscopic observations made on days 0, 5, 10, and 15. By day 5, all groups did not exhibit accelerated wound closure. However, by day 10, while the control group had not healed completely, the P&G group showed a wound closure rate approximately 9 % faster than the control group, highlighting the contractile P&G hydrogel's enhancement of wound contraction, with the P&G@LMs group achieving a higher healing rate of 68 % (Fig. 8C and D). Moreover, by day 15, the wound closure rates between the control and P&G groups were comparable, both around 63 %, but the LMs group and P&G@LMs group had higher healing rates than the control group, with the P&G@LMs group reaching up to 76 % healing. Notably, the scar area in the P&G@LMs group was approximately 40 % less than that in the control group (Fig. 8E), emphasizing the significant enhancement of wound healing and skin regeneration facilitated by the contractile P&G@LMs hydrogel.

2.7. Evaluation of the inflammatory microenvironment and fibrosis in the regenerated skin

To investigate the internal condition of the regenerated skin, tissue samples from all experimental groups were collected on day 15 and subjected to hematoxylin and eosin (H&E) staining for detailed histological analysis. As illustrated in Fig. 8F and G, there were no significant differences in scar widths between the control and P&G groups, both displaying considerable infiltration of inflammatory cells (indicated by blue arrows). In contrast, the LMs and P&G@LMs groups showed a marked reduction in scar widths and decreased inflammatory cell infiltration, underscoring the anti-inflammatory properties of LMs (ACEI). At the end of the animal study, the biosafety of all groups was assessed. Following 15 days of treatment, key organs including the heart, liver, spleen, lungs, and kidneys were subjected to H&E staining. Pathological examination revealed no abnormal changes in the tissue structures of these organs (Fig. S10, Supporting Information).

To elucidate the inflammatory conditions observed in the H&E staining, further analysis was conducted using immunofluorescence. Fig. 8H–J revealed that the control group manifested the most pronounced expression of CD86 and a reduced expression of CD206 within the regenerated skin, indicating an ongoing inflammatory microenvironment. Conversely, the application of P&G hydrogel, which ameliorated inflammatory responses and oxidative stress, resulted in decreased CD86 expression and enhanced CD206 expression in the regenerated skin of the P&G group. These results were consistent with our previous cellular experiments (Fig. 6), demonstrating that P&G hydrogel effectively reduced polarization towards the pro-inflammatory M1 phenotype and promoted some polarization towards the anti-inflammatory M2 phenotype, thereby supporting the transition from the inflammation to the proliferation phase in wound healing. Moreover, the introduction of LMs (ACEI) led to a further reduction in the expression of both CD86 and CD206 in the LMs group. Given that the P&G@LMs group experienced the most prolonged local exposure to ACEI, it exhibited the lowest levels of CD86 and CD206, demonstrating that the regenerated skin with ACEI application had exited the inflammatory microenvironment. Meanwhile, we detected the expression of the inflammatory factor TNF-α in all groups, and the expression of TNF-α was the least in the P&G@LMs group (Fig. 8H and K). These results further highlighted the precise

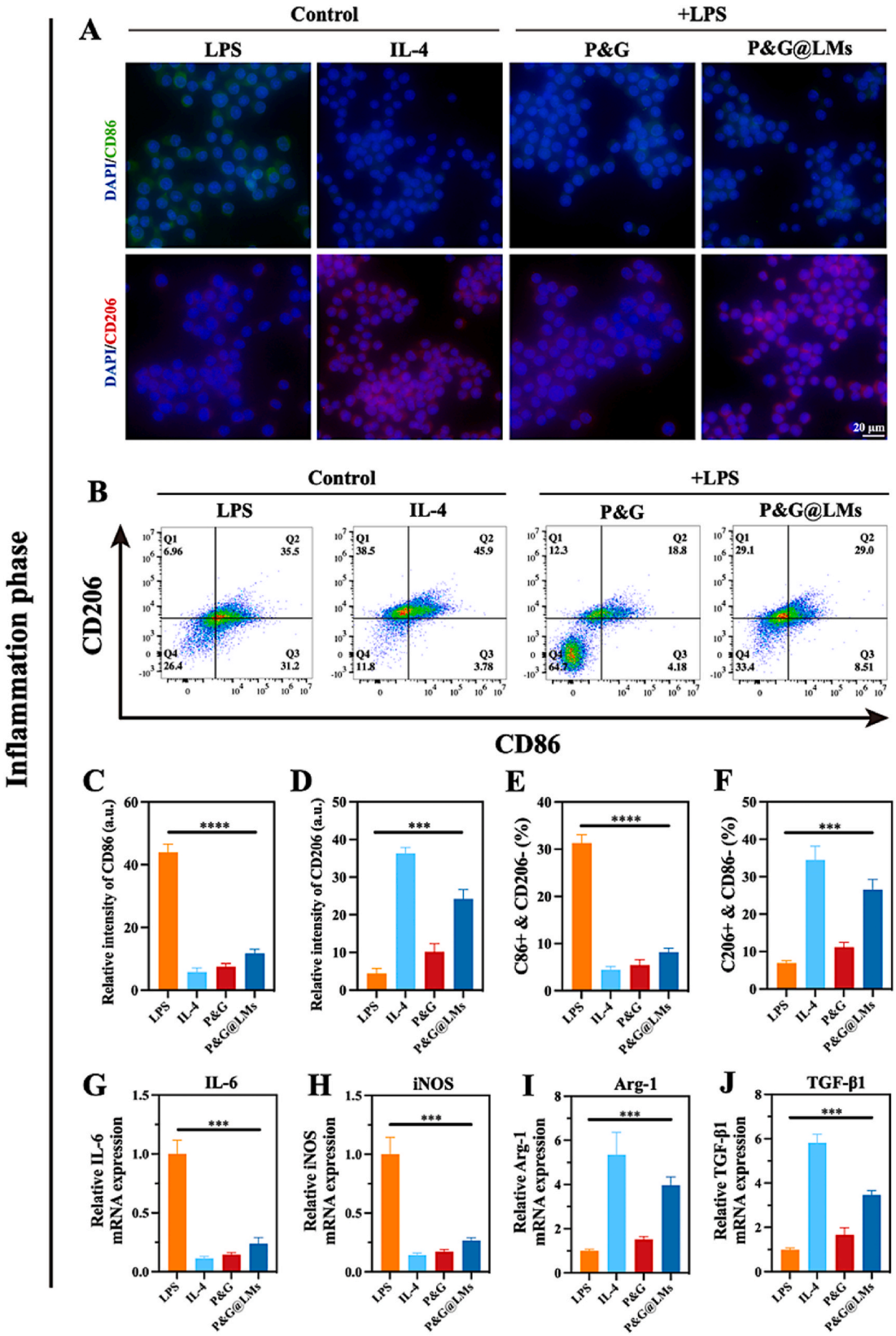

Fig. 6. Inflammatory modulation capacity of P&G and P&G@LMs in vitro. A) Depiction of CD86 (green) and CD206 (red) differentiation markers in RAW 264.7 macrophages treated with LPS (positive control), IL-4 (negative control), P&G, and P&G@LMs via fluorescence microscopy. B) Flow cytometry results showing the CD86 and CD206 expression in RAW 264.7 macrophages treated with LPS (positive control), IL-4 (negative control), P&G, and P&G@LMs. C-D) Quantitative statistics of the relative fluorescence intensity of CD86 and CD206 (n = 3). Statistical histogram of E) M1 (CD86+CD206-) and F) M2 (CD206+CD86-) type macrophages ratio after treated with LPS (positive control), IL-4 (negative control), P&G, and P&G@LMs (n = 3). G-J) Relative mRNA expression of IL-6, iNOS, Arg-1, and TGF-β1 in RAW 264.7 macrophages treated with LPS (positive control), IL-4 (negative control), P&G, and P&G@LMs (n = 3). Error bars represent the mean ± standard deviation. *P < 0.05; **P < 0.01; ***P < 0.001; ****P < 0.0001; NS, not statistically significant.

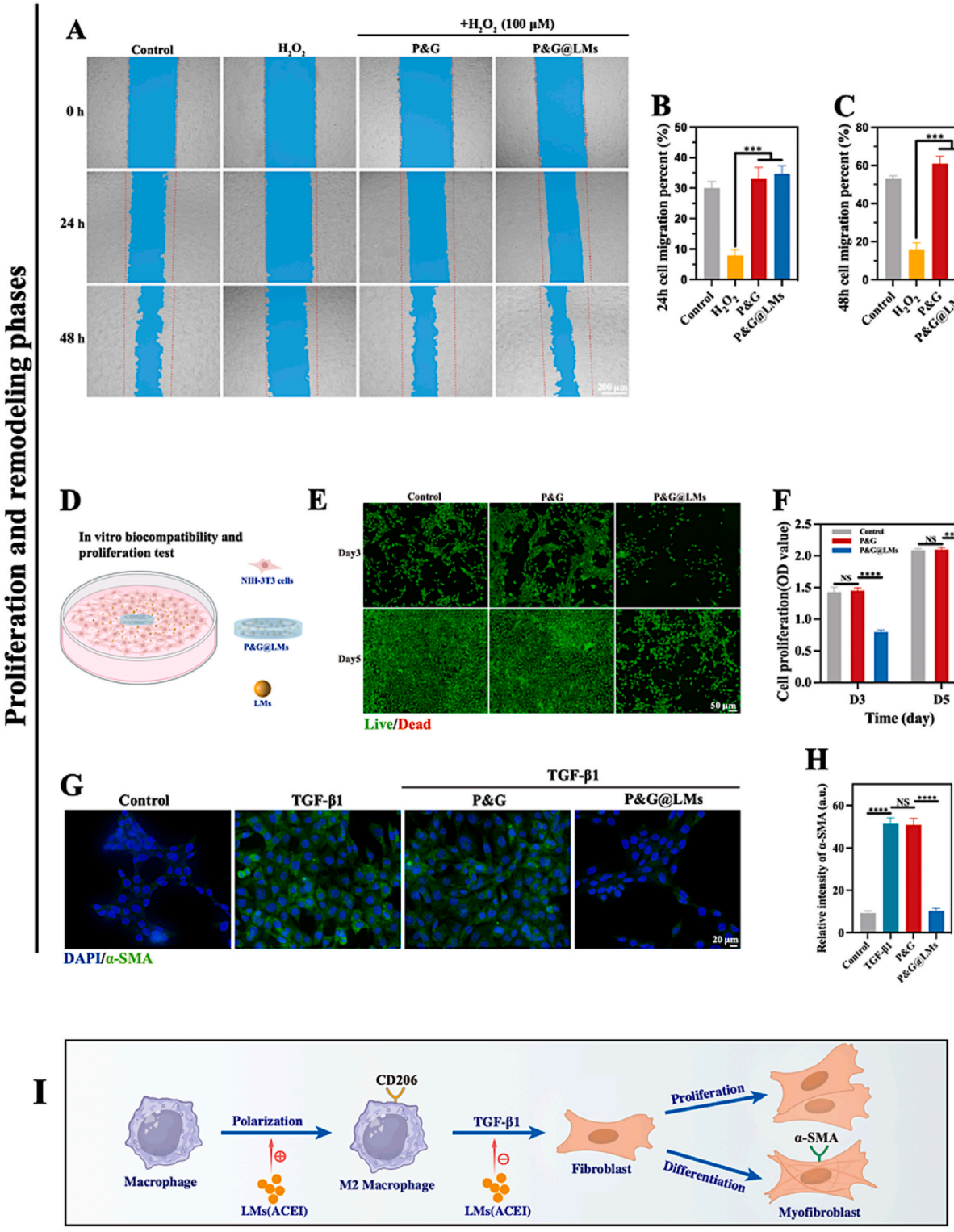

Fig. 7. Regulation of cellular migration, proliferation, and differentiation by P&G and P&G@LMs in vitro. Scratch assay images A) and quantitative migration ratio B, C) of HaCaT cells after treated with H_2O_2, P&G, and P&G@LMs for different times (n = 3). scale bar = 200 μm. D) Schematic illustration of co-culture of NIH-3T3 cells with P&G@LMs. E) Live/Dead staining of NIH/3T3 after co-culture with P&G and P&G@LMs for different times (scale bar = 50 μm). F) Proliferation of NIH/3T3 incubated for 3 and 5 days by MTT assay (n = 3). G) Depiction of α-SMA expression in NIH/3T3 cells treated with PBS (control), TGF-β1, P&G, and P&G@LMs via fluorescence microscopy (scale bar = 20 μm). H) Quantitative statistics of the relative fluorescence intensity of α-SMA (n = 3). I) Schematic illustration of the regulatory effects of LMs (ACEI) on macrophages and fibroblasts. Error bars represent the mean ± standard deviation. *P < 0.05; **P < 0.01; ***P < 0.001; ****P < 0.0001; NS, not statistically significant.

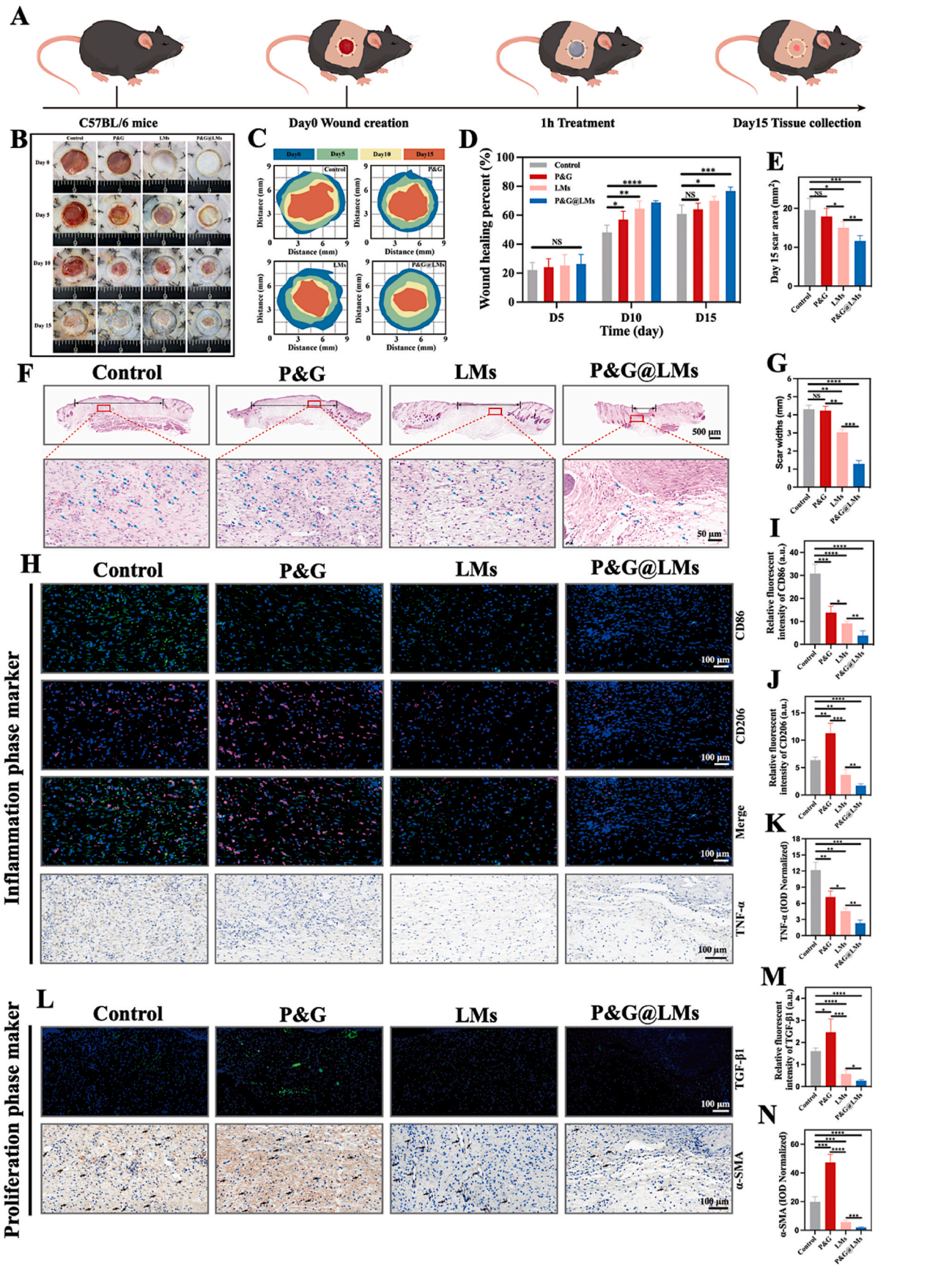

(caption on next page)

Fig. 8. Therapeutic effects of P&G and P&G@LMs on skin regeneration. A) Schematic diagram depicting the experimental protocol in C57BL/6 mice. B) Representative images of the wound healing and skin regeneration in mice treated with Control, P&G, LMs, and P&G@LMs on day 0, 5, 10, and 15. C) Schematic diagram of the skin regeneration process during 15 days. D) Quantitative data of the relative wound closure percent at different time points (n = 5). E) Quantitative data of the relative scar area on day 15 (n = 5). F) H&E staining of the regenerated tissues on day 15. Double-headed arrow: scar width. Blue arrow: inflammatory cell (upper scale bar = 500 μm; lower scale bar = 50 μm). G) Quantification of the widths of scar (n = 3). H) and L) Immunofluorescence (CD86, CD206, and TGF-β1) and immunohistochemical (TNF-α and α-SMA) staining at the regenerated area to evaluate the inflammation and fibrosis (scale bar = 100 μm). I), J) and M) Quantitative statistics of the relative fluorescence intensity of CD86, CD206, and TGF-β1 (n = 4). K) and N) Quantitative statistics of the relative expression of TNF-α and α-SMA (n = 4). Error bars represent the mean ± standard deviation. *P < 0.05; **P < 0.01; ***P < 0.001; ****P < 0.0001; NS, not statistically significant.

spatiotemporal modulation of drug release by P&G@LMs and its profound impact on managing the inflammatory microenvironment.

Notably, during the transition from the inflammation to the proliferation phase of wound healing, M2 macrophages induce and sustain a profibrotic niche through TGF-β1 secretion, which drives the differentiation of fibroblasts into the highly contractile α-SMA-positive myofibroblasts, leading to collagen stiffening and mediating fibrotic repair [14,15]. To this end, we used immunofluorescence and immunohistochemistry to further assess the activity of myofibroblasts and the extent of fibrosis within the regenerated skin, focusing specifically on α-SMA and TGF-β1 expression. As shown in Fig. 8L–N, the control group exhibited lower expressions of TGF-β1 and α-SMA within the inflammatory environment. Conversely, the P&G group, benefiting from the hydrogel's ability to modulate the inflammatory environment, showed heightened expression of both markers. These findings were consistent with characteristics of fibrotic repair, indicating prevalent M2 macrophages and the highly contractile α-SMA-positive myofibroblasts [14,15], suggesting that while the contractile P&G hydrogel facilitated initial wound healing, it did not alter the trajectory of fibrotic repair. With the application of LMs (ACEI) and extended duration, their expression significantly reduced in the P&G@LMs group, aligning with our previous cellular experiments (Figs. 6 and 7). This highlighted the spatiotemporal release of ACEI by P&G@LMs, which could, to some extent, inhibit the excessive proliferation of fibroblasts and their differentiation into the highly contractile α-SMA-positive myofibroblasts. Moreover, α-SMA not only marks contractile myofibroblasts but also vascular smooth muscle cells. As indicated by black arrows in Fig. 8L, a decrease in internal vasculature was noted in the P&G@LMs group. The results in the P&G@LMs group were similar to the normal skin regeneration during the remodeling phase, characterizing by the extensive cellular apoptosis, including endothelial cells, macrophages, and myofibroblasts [2]. The results indicated that P&G@LMs could promote skin regeneration.

2.8. Evaluation of collagen deposition and biological orientation in regenerated skin

It is noteworthy that collagen deposition and arrangement play critical roles in the skin's architecture, with type I collagen primarily responsible for maintaining mechanical stability and type III collagen providing elasticity, these collagens are intertwined into a basket-like weaving structure, which is foundational to the biomechanics of normal dermis [74,75]. However, it is known that the highly contractile α-SMA-positive myofibroblasts produce less collagen [14,15]. To clarify the collagen deposition within the regenerated skin of each group, we used Masson's trichrome staining for further analysis. As shown in Fig. 9C and I, both the control and P&G groups showed comparably low total collagen volume fractions, with no significant difference between them. The LMs group showed a slight increase, while the P&G@LMs group exhibited the highest collagen deposition, approximately 2.5 times that of the control group. A closer examination of the central internal areas of each group (Fig. 9B) revealed that the regenerated skin in the control and P&G groups contained lesser collagen, presumably due to the presence of numerous highly contractile α-SMA-positive myofibroblasts. But with the application of LMs (ACEI) and the extended duration, fibroblasts were able to maintain the immaturity and a lower differentiation state, thereby normally secreting collagen.

However, due to the complex structure of collagen, which cannot be analyzed using conventional Euclidean geometry, we employed fractal analysis to quantify the inherent irregularity of collagen organization across different groups [55]. In this analysis, fractal dimension and lacunarity values quantitatively assessed the complexity of collagen arrangement using the Fractal Analysis plugin in ImageJ [55]. After binarizing the images from Fig. 9B to create Fig. 9A, we conducted statistical analysis on the binary image's fractal dimension and lacunarity. As shown in Fig. 9G and H, the control and P&G groups exhibited lower fractal dimension and increased lacunarity, with no significant differences between them. The LMs group and the P&G@LMs group showed increased fractal dimension and decreased lacunarity, with the P&G@LMs group reaching a fractal dimension as high as 1.98. These results indicated that the more regenerated the skin (P&G@LMs group), the more complex the arrangement of collagen within it, with higher fractal dimension and lower lacunarity, approaching a two-dimensional plane and making the entire plane smoother.

Interestingly, we also observed distinct boundaries between the fibrotic repair and the regenerated normal skin in the control, P&G, and LMs groups, while these boundaries were relatively blurred in the P&G@LMs group (Fig. 9D). This indicated that the fibrotic repair was significantly suppressed in the P&G@LMs group, leading to the highest degree of normal skin regeneration. Current studies have demonstrated that wound healing progresses from the periphery towards the center and from the bottom layer upwards [54,55]. In our study, the P&G@LMs hydrogel's layer-by-layer degradation and phased release correlated spatiotemporally with wound healing process, with the tissue at the wound's periphery being the first to be affected by LMs (ACEI). To better assess the overall condition of the regenerated skin, Picrosirius Red staining and polarization microscopy were used to analyze the collagen deposition and arrangement in the regenerated normal skin. As shown in Fig. 9E, type I collagen tended to appear red, while type III collagen appeared green. The collagen deposition across the four groups (Fig. 9J) was roughly similar to the overall collagen deposition (Fig. 9I). Notably, compared to the other three groups, the P&G@LMs group showed a significant increase in type I collagen deposition (Fig. 9K) and a notable decrease in type III collagen deposition (Fig. 9L), which aligned with the characteristics of the remodeling phase, where the secretion of type I collagen increases and gradually replaces type III collagen [2]. Furthermore, recent study has reported that in C57BL/6 mice aged 0–9 weeks, the ratio of type I to type III collagen in normal skin increases from 1.3:1 to 4.5:1 [74]. In our study using 8-week-old C57BL/6 mice, by the time we collected the samples, the mice were aged 10–11 weeks, and the ratio in the normal skin was approximately 4.54:1 while the ratio in the P&G@LMs group's regenerated normal skin reached 1.74:1, far exceeding the other three groups (Fig. 9M and Fig. S11, Supporting information). This again confirmed that the application of P&G@LMs could promote the normal regeneration of skin.

At the same time, to more precisely analyze whether the regenerated skin's collagen after the application of P&G@LMs had a biomechanical basis, we utilized orientation analysis using the OrientationJ plugin in ImageJ to objectively demonstrate the collagen orientation in the regenerated normal skin [76]. By transforming the vector data from Fig. 9F into a waveform graph (Fig. 9N and Fig. S11, Supporting information), it became apparent that the control and P&G groups, characterized by a lesser quantity of type I collagen, predominantly exhibited a unimodal distribution of type III collagen orientation. Conversely, in the

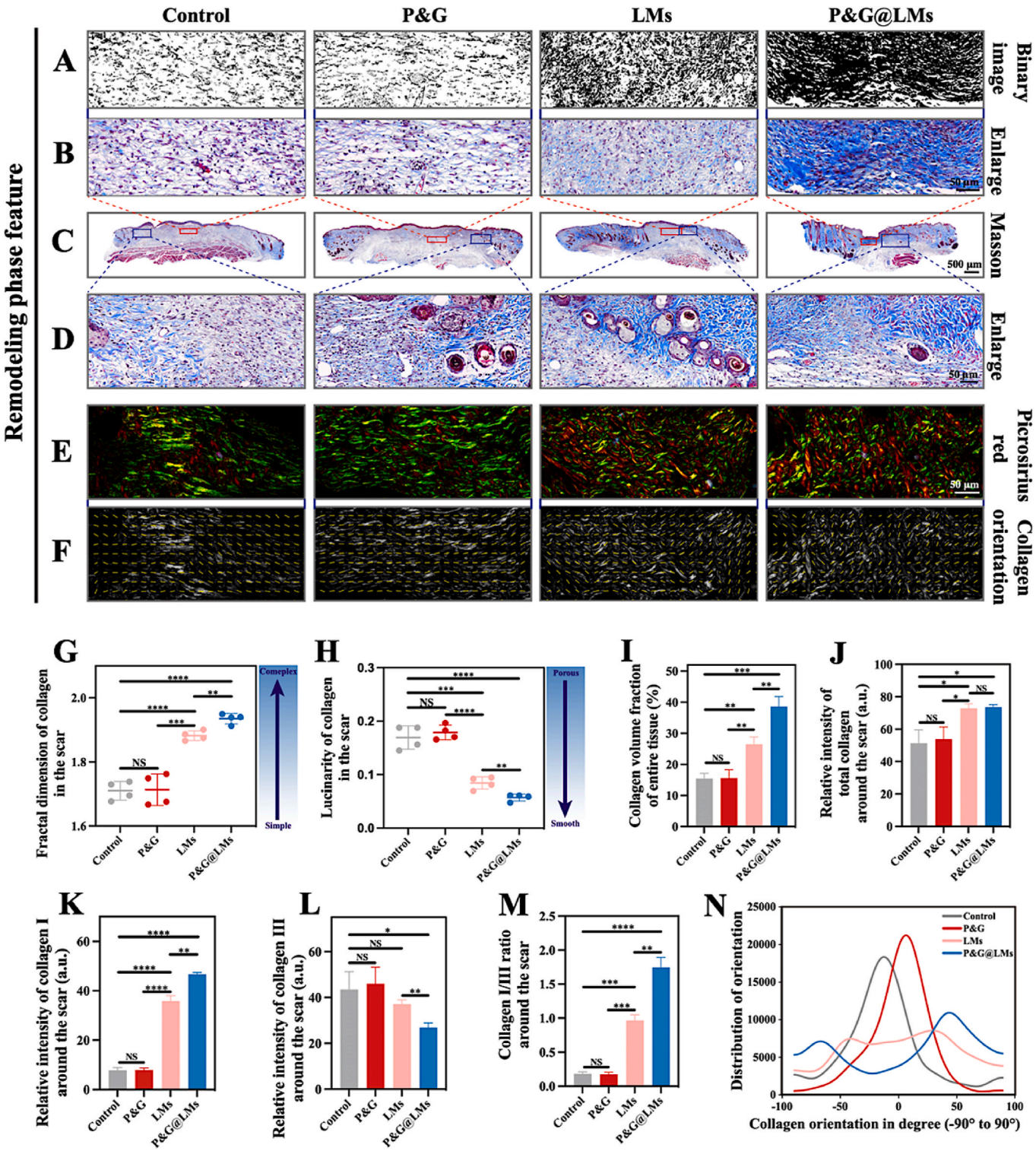

Fig. 9. Analysis of the effects of P&G and P&G@LMs on skin regeneration. C) Masson's trichrome staining of the entire regenerated tissues on day 15 (scale bar = 500 μm). B) and D) Magnified images of different parts of the regenerated tissues (scale bar = 50 μm). A) Binary images of B). E) Picrosirius red staining of the collagen in the scar-surrounding normal regenerated skin on day 15 (scale bar = 50 μm). F) Vector field images of collagen from E). G-H) Fractal dimension and lacunarity analysis of collagen (n = 4). I-J) Statistical analysis of collagen deposition in the entire regenerated tissues and the scar-surrounding normal regenerated skin (n = 4). K-M) Statistical analysis of the collagen I and collagen III in the scar-surrounding normal regenerated skin (n = 4). N) Orientation analysis of the collagen I and collagen III in the scar-surrounding normal regenerated skin. Error bars represent the mean ± standard deviation. *P < 0.05; **P < 0.01; ***P < 0.001; ****P < 0.0001; NS, not statistically significant.

LMs and P&G@LMs groups, the enhanced presence of type I collagen, in conjunction with type III collagen, contributed to a complex weaving network, resulting in a bimodal distribution (Fig. 9N and Fig. S11, Supporting information Fig. S11). These findings highlighted the spatiotemporal correlation between P&G@LMs' layer-by-layer degradation and phased release with the dynamics of skin regeneration. The gradual delivery of therapeutic agents could more precisely match the diverse demands of each phase in skin regeneration, optimizing therapeutic outcomes and fostering the alignment of collagen in the regenerated skin toward a biomechanical orientation.

3. Conclusions

In summary, we developed a novel hydrogel system (P&G@LMs), composed of modified gelatin/PF127 and ACEI-loaded microspheres (LMs) without any crosslinking agents. The contractile P&G hydrogel facilitated an early wound contraction and healing, but did not affect the fibrotic repair after healing. The ACEI released from LMs also promoted wound healing, associated with the modulation of macrophage polarization during the inflammation phase. However, the later weakening of skin regeneration by LMs alone was due to the lack of an appropriate carrier to fix the LMs at the wound site to prolong their action period. Yet, embedding LMs into the P&G hydrogel to form the P&G@LMs system maximized their synergistic effect, not only promoting wound healing but also enhancing the effect of promoting skin regeneration. P&G@LMs possessed properties crucial for versatile modulation of the wound microenvironment and promotion of skin regeneration, including tissue adhesion, self-contraction, water-retention, anti-swelling, spatiotemporal drug release, anti-inflammation, anti-oxidation, anti-fibrosis, and biomechanically mimetic mechanical properties. Specifically, upon application to a skin wound, P&G@LMs could immediately achieve hemostasis, then cleared ROS and inflammatory factors from the microenvironment, and promoted wound closure. The spatiotemporally released LMs (ACEI) promoted polarization of macrophages towards the anti-inflammatory M2 phenotype during the inflammation phase, accelerating the transition from inflammation to proliferation. Meanwhile, P&G@LMs could, to some extent, inhibit the excessive proliferation and differentiation of fibroblasts into the highly contractile α-SMA-positive myofibroblasts in the proliferation and remodeling phases through four aspects, so as to maintain the immaturity and a low differentiation state of fibroblasts, thus regulating the fibrotic repair. The continued release of LMs (ACEI) could somewhat inhibit excessive fibroblast proliferation and regulate the macrophage-induced profibrotic niche's impact on fibroblast differentiation. The hydrogel's self-shrinkage property could mimic the contractile feature of myofibroblasts, and its skin-like elastic modulus could accommodate the skin dynamic changes and restore the mechanical integrity of the wound defect, thereby partially substituting the mechanical role of the highly contractile α-SMA-positive myofibroblasts in tissue repair. These biomimetic features provided an advanced bioengineering solution to the complex biomechanical environments, optimizing the healing process and tissue regeneration. Importantly, P&G@LMs also promoted the normal biomechanical orientation of collagen in the regenerated skin. Therefore, as a dressing for wound healing, P&G@LMs took promise as an ideal biomaterial for promoting skin regeneration.

4. Experimental section

4.1. Materials and reagents

Pluronic F-127(PF127, ~12,600 g/mol) and gelatin (type A, 50 KDa-100 KDa) were purchased from Sigma-Aldrich. 4-Formylbenzoic acid and 4-Dimethylamino-pyridine (DMAP) were purchased from Macklin (Shanghai, China). 1-hydroxybenzotriazole (HOBt), carbonic dihydrazide (CDH), 1-(3-Dimethylaminopropyl)-3 ethylcarbodiimid hydrochloride (EDC.HCl), lisinopril, hydrogen peroxide (H_2O_2), dichloromethane (DCM) and dimethyl sulfoxide (DMSO) were purchased from Aladdin (Shanghai, China). Poly (lactic-co-glycolic acid) (PLGA, 50:50 ratio of PLA/PGA) was provided by Jinan Daigang Biological Technology Co., Ltd. China. Polyvinyl alcohol (PVA) was supplied by Shin-Etsu Chemical Co., Ltd. Japan. DCFH-DA probe, 1, 1-diphenyl-2-trinitrophenylhydrazine (DPPH), 3-(4,5-Dimethylthiazol-2-yl)-2,5-diphenyl tetrazolium bromide (MTT), lipopolysaccharide (LPS), Calcein AM and propidium iodide (Cell Live/Dead kit) were purchased from Solarbio (Beijing, China). Dulbecco's modified Eagle's medium and fetal bovine serum (FBS) were purchased from Gibco (Carlsbad, CA, USA). Neonatal Calf Serum was purchased from VivaCell (Shanghai, China). Endothelial cell medium (ECM) was purchased from ScienCell (San Diego, USA). HaCaT cell and Human Umbilical Vein Endothelial Cell (HUVEC) were purchased from Suzhou Haixing Biology Technology Co., Ltd. China. Raw 264.7 cell and NIH-3T3 cell were purchased from Wuhan Procell Life Science&Technology Co., Ltd. China. APC anti-mouse CD86 antibody and PE anti-mouse CD206/MMR antibody were purchased from Elabscience (Wuhan, China). Other antibodies were purchased from Proteintech (Wuhan, China). IL-4 was purchased from PeproTech, Inc (NJ, USA).

4.2. Synthesis of benzaldehyde-modified Pluronic F-127 (PF127-CHO)

According to the previous literature [47], 10g PF127 was placed in a 250 mL flask, dried through azeotropic distillation with toluene, and then 50 mL of anhydrous dichloromethane was added to dissolve the reagent. Following this, 1.6g 4-formylbenzoic acid was dissolved in 5 mL of anhydrous dichloromethane, and 2.5g 1-ethyl-(3-dimethylaminopropyl) carbodiimide hydrochloride (EDC.HCl) was added to activate the carboxylate group for 15 min. Subsequently, 1.6g 4-dimethylaminopyridine (DMAP) was added to further activate the carboxylate group for an additional 15 min. The activated 4-formylbenzoic acid solution was then slowly dripped into the PF127 solution. After the reaction at room temperature for 24 h, the dichloromethane was removed by rotary evaporation. Next, 100 mL of deionized (DI) water was added to dissolve the precipitate. Finally, the solution was placed in a dialysis bag (MWCO 8–14 kDa) and dialyzed in DI water for 3 days to obtain PF127-CHO monomer by freeze-drying.

4.3. Synthesis of carbonic dihydrazide (CDH)-modified gelatin (Gel-CDH)

According to the previous literature [48], 3g gelatin (1 % w/v) was dissolve in 300 mL of DI water at 40 °C. Added 0.45g EDC.HCl dissolved in 10 mL of deionized water (4.5 % w/v), and 0.45g 1-hydroxybenzotriazole monohydrate (HOBt) dissolved in 10 mL of dimethyl sulfoxide (DMSO) (4.5 % w/v) to activate the carboxyl group for 30 min. Then, added 2.2g CDH (0.73 % w/v). The pH of the solution was adjusted to 5.2 and the reaction was maintained overnight at room temperature. Finally, the solution was placed in a dialysis bag (MWCO 8–14 kDa) and dialyzed in DI water for 3 days to obtain Gel-CDH monomer by freeze-drying.

4.4. Synthesis of lisinopril-microspheres (LMs)

According to the previous literature [51], LMs were synthesized using a water-in-oil-in-water (W1/O/W2) double emulsion solvent evaporation method. Initially, 50 mg lisinopril was dissolved in 1 mL of 5 % w/v polyvinyl alcohol (PVA) solution, serving as the internal water phase W1. Simultaneously, 0.5g PLGA was dissolved in 5 mL of dichloromethane (DCM) as the oil phase O, and 100 mL of 5 % w/v PVA solution was prepared as the external water phase W2. Initially, W1 was added to O, forming the first emulsion (W1/O) via ultrasonic emulsification with a probe in an ice water bath for 6 min (working 3s, resting 3s, 200 W). Subsequently, the W1/O emulsion was stirred in an ice water

bath at 20000 rpm using a homogenizer for 3 min. The resulting W1/O emulsion was slowly injected into 50 mL of external aqueous phase W2 using a syringe, while stirring at 10000 rpm with a homogenizer, and further emulsified at 20000 rpm for 3 min to create the W1/O/W2 emulsion. To expedite the diffusion rate of DCM from W1/O to W2, an additional 50 mL of external aqueous phase W2 was introduced to the W1/O/W2 emulsion system under magnetic agitation. Continuous agitation at 40 °C atmospheric pressure for 2 h ensured complete DCM evaporation, preventing the formation of pores on the microspheres' surface. As DCM diffused from W1/O to W2 and evaporated, the emulsion gradually solidified. The resulting mixture was then centrifuged at 4000 rpm for 10 min to obtain milky microspheres, which were subsequently washed three times with DI water and freeze-dried to yield LMs. The final product was stored in a dryer at −20 °C. The drug loading rate (LR) and encapsulation rate (ER) were calculated using the following formulas: Drug loading rate = the loaded lisinopril mass/the total mass of microsphere * 100 %, Encapsulation rate = the loaded lisinopril mass/the total drug mass * 100 %.

4.5. Synthesis of PF127-CHO/gel-CDH (P&G) hydrogel and P&G hydrogel loaded with LMs (P&G@LMs)

2.5g PF127-CHO monomer was dissolved in 10 mL of phosphate-buffered saline solution (PBS) to yield a 25 % w/v PF127-CHO solution, while 0.8g Gel-CDH monomer was dissolved in 10 mL of PBS to obtain an 8 % w/v Gel-CDH solution. The total volume of hydrogel was set to 900 μL, and PF127-CHO and Gel-CDH were then thoroughly mixed in a double-channel connector for 30 s at room temperature, following the volume ratios (PF127-CHO: Gel CDH) of 1:2, 1:3, and 1:4 to produce P&G2, P&G3, and P&G4 hydrogel, respectively. Subsequently, P&G sol were mixed completely with LMs powder prior to gel formation to obtain P&G@LMs. This procedure was designed to minimize the aldol condensation reaction between the hydroxy group on PLGA and the aldehyde group on PF127-CHO. The chemical structure of P&G hydrogels was confirmed using FTIR analysis.

4.6. Characterization of synthetic materials

The chemical structures of PF127, PF127-CHO, gelatin, Gel-CDH, and P&G were analyzed using Fourier Transform Infrared Spectroscopy (FTIR, Nicolet iS50, Thermo Fisher, USA). The microscopic morphology of P&G, LMs, and P&G@LMs was observed via field emission Scanning Electron Microscopy (SEM, SU-8010, Hitachi, Japan) at 3 kV.

4.7. Swelling rate test

The swelling behavior of the hydrogel was assessed using gravimetric analysis. Briefly, freshly prepared samples of P&G and P&G@LMs (300 μL each) were immersed directly in PBS (pH 7.4) at 37 °C. At predetermined time intervals (2, 4, 8, 12, and 24 h), the samples were removed, excess surface moisture was blotted using filter paper, and then they were accurately weighed and photographed to determine the extent of swelling. The swelling rate (SR, %) was calculated using the formula: SR (%) = (Ws-W0)/W0*100 %, where Ws represents the weight after swelling and W0 represents the initial weight. Each group was measured in triplicate.

4.8. Degradation rate test

300 μL of freshly prepared P&G or P&G@LMs were incubated in PBS at 37 °C. At predetermined intervals, the solution was removed, and the remaining hydrogel was freeze-dried for 12 h and weighed to calculate the amount of degradation. The degradation of the hydrogels was calculated using the following formula: weight remaining (%) = Wt/W0 × 100 %, where Wt and W0 represent the dry weight of the remaining hydrogel at different time points after degradation and the initial dry weight of the hydrogel, respectively. Each group was measured in triplicate.

4.9. Lisinopril release test

First, the maximum absorbance of the standard lisinopril solution at 200 nm–400 nm was determined using a UV–vis spectrophotometer (UV-3150, Japan), and it was found that the solution had the maximum absorbance at 210 nm. Then, lisinopril's standard curves were plotted according to different solution concentrations, and linear regression equations were derived. Freshly prepared P&G@Lis, LMs, and P&G@LMs (all containing equal amounts of lisinopril) were immersed in 37 °C PBS (pH 7.4) and incubated at an oscillating speed of 100 rpm for 8 days at predetermined intervals. A 100 μL sample of PBS was analyzed using a UV–vis spectrophotometer and replaced with an equivalent fresh PBS solution. Each group was measured in triplicate.

4.10. Compression test

The P&G and P&G@LMs samples were prepared as cylinders (10 mm in height x 10 mm in diameter), and compression stress-strain tests were conducted at 25 °C. The universal material testing machine (Zwick/Roell Z020) was utilized for the test. The preload was set at 0.01 N, with a compression strain rate of 1 mm/min, and compression was halted when the strain level reached 80 % of the original height. The compression modulus was determined by calculating the slope of the linear segment of the stress-strain curve within the 10%–20 % strain range. Each group was measured in triplicate.

4.11. Tensile test

The mechanical tensile stress-strain assessment was conducted through a uniaxial tensile test using a universal material testing machine (Zwick/Roell Z020) equipped with a 100 N tension sensor at 25 °C. P&G and P&G@LMs samples were prepared into elongated dumbbell specimens (4 mm thick, 50 mm total length, the end width was 8 mm, with the narrowest part measuring 20 mm in length and 4 mm in width). The tensile strain rate was set at 10 mm/min, and the tensile modulus was determined by calculating the slope of the linear segment of the stress-strain curve within the 10%–20 % strain range. Each group was measured in triplicate.

4.12. Rheological test

The rheometer was utilized to assess the rheological behavior of hydrogel at 37 °C using parallel plates with a diameter of 20 mm and a 1 mm gap. The rheological parameters measured were the energy storage modulus (G′) and the loss modulus (G″). Initially, a frequency sweep test was conducted between 0.1 and 10 Hz under constant strain (1 %), and the average G′ at 1 Hz was calculated to evaluate the rheological mechanical properties of the hydrogel. Subsequently, the shear thinning property of the hydrogel were evaluated at shear rates ranging from 0.1 to 1000 s^{-1}. Following this, a strain amplitude sweep test (strain % (γ) = 0.1–1000 %) was performed to determine the critical strain point. Finally, the hydrogel's ability to recover from strain deformation was measured by subjecting it to repeated exposure to 1 % and 500 % oscillatory strain every 200 s at a frequency of 1 Hz. Each group was tested in triplicate.

4.13. Adhesion test

The adhesive ability of the hydrogel to wet tissue was quantitatively measured using a lap shear test conducted on fresh porcine skin. Fresh porcine skin was purchased from local supermarket and stored in a −20 °C refrigerator before use. To prepare the lap shear test sample, the

porcine skin was first thawed for 2 h and then cut into slices measuring 4.5*2*0.5 cm. Following this, 200 μL of P&G and P&G@LMs were applied to the surface of the porcine skin and spread using a scalpel to cover a 2*1 cm area. Another piece of pig skin was immediately pressed onto the hydrogel-covered pig skin, and the two pieces of skin were pressed together with a load of 200g. The assembly was then placed in an incubator at 37 °C for 30 min. The lap shear test (Zwick/Roell Z020) was performed using a 100 N load cell at a strain rate of 1 mm/min. The adhesive strength was calculated as the maximum stress divided by the adhesive area. Each group was tested in triplicate.

4.14. Water-retention test

The water evaporation method was employed to simulate and verify the hydrogel's ability to maintain moisture after sealing the wound. 3 mL of methylene blue-stained PBS solution was added to 5 mL glass vials, and the total weight of each vial containing PBS was measured. The vials were randomly divided into four groups: uncovered group (positive control), cling film group (negative control), P&G group, and P&G@LMs group. The cling film group was covered with commonly used food-grade cling film, sealed at the edges where the wrap contacted the glass vial using the sealing film. The P&G and P&G@LMs groups had their openings sealed with 500 μL of hydrogel. The four groups of vials were then placed in a 37 °C environment. After 48 h, the total weight of each vial was measured again. The water-retention rate of the hydrogels was calculated using the following formula: water-retention rate (%) = Wr/W0 × 100 %, where Wr and W0 represent the remaining total weight after 48 h and the initial total weight, respectively. Each group was measured in triplicate.

4.15. Coagulation test

The hemostatic potential of the hydrogel was assessed using a rat liver hemorrhage model. In simple terms, 6-week-old SD rats were induced and maintained under anesthesia using isoflurane, then immobilized on a surgical plate. The rat liver was exposed through an abdominal incision, and the serous fluid around the liver was carefully removed. A sheet of pre-weighed filter paper on a paraffin film was placed under the liver. Next, an open wound approximately 1.6 mm in diameter was created on the liver using a syringe needle, and a 100 μL hydrogel was promptly applied to the bleeding site with a syringe. After 60 s, the amount of blood lost was recorded based on the weight of the filter paper. Untreated rats served as the blank control group. Each group was tested in triplicate.

4.16. Hemolysis test

Whole blood containing citric acid (CWB) was centrifuged at 3000 rpm for 5 min and washed to isolate red blood cells (RBCs). Then, 100 μL of RBCs was added to 2 mL of PBS to obtain a 5 % RBC suspension. P&G and P&G@LMs were ground into powder using liquid nitrogen, and 10 mg of sample powder was added to 800 μL of PBS and mixed with 200 μL of RBC suspension. PBS and DI water (800 μL) were used as negative control and positive control, respectively. The mixture was co-cultured at 37 °C for 1 h and photographed. Subsequently, the samples were separated by centrifugation at 3000 rpm for 5 min, and the absorbance of the supernatant at 540 nm was measured using a spectrophotometer (Multiskan FC, Thermo Fisher, America). RBC hemolysis was calculated as follows: Hemolysis rate (%)=(Ah - Ap)/(Ad - Ap) × 100 %, where Ah represents the absorbance of the hydrogel group, Ap represents the absorbance of the PBS group, and Ad represents the absorbance of the DI water group. Each group was measured in triplicate.

4.17. In vitro biocompatibility test of materials

4.17.1. In vitro cytocompatibility of monomer polymer

To assess the monomer polymer's cytotoxicity, HUVEC and NIH-3T3 cells were seeded into 96-well plates at an initial density of 8000 cells per well and incubated at 37 °C for 24 h. The medium was then replaced with 200 μL of medium containing different concentrations of Gel-CDH and PF127-CHO (1000 μg/mL, 500 μg/mL, 250 μg/mL, 125 μg/mL, 62.5 μg/mL). After 24 h of co-culture, following the manufacturer's instructions, 10 μL of MTT solution (5 mg/mL) was added to each well and incubated at 37 °C for 3–4 h. Subsequently, the co-culture solution was aspirated, and 300 μL of DMSO was added to dissolve the formed crystals. Then, 200 μL of the supernatant was transferred from each well to another 96-well plate. Absorbance was measured at 490 nm to assess cell viability. Each group was measured in triplicate.

4.17.2. In vitro cytocompatibility of synthetic materials

Based on previous studies, the in vitro cell experiments have shown that 10 μM of ACEI can inhibit fibroblasts to a certain extent, while 100 μM excessively inhibits their proliferation and differentiation [31,69]. Therefore, we selected concentrations between 10 μM and 100 μM to study the effects on cells. Our microspheres had a drug loading rate of approximately 4.5 %. We mixed 40 mg of LMs with 900 μL of P&G to prepare 25 μL of P&G@LMs hydrogel discs for cellular experiments. Theoretically, the final concentration of ACEI released upon the complete degradation of P&G@LMs was about 113 μM. Considering the sustained release properties of P&G@LMs, the concentration of ACEI in the cell culture medium on the first day was approximately 30.5 μM. NIH-3T3 cells (500 μL) were seeded into 24-well plates at an initial density of $2*10^4$ cells per well and incubated at 37 °C for 24 h to allow for cell adhesion, and then 500 μL of medium was added to each well. Subsequently, either 25 μL of P&G or 25 μL of P&G@LMs hydrogel discs prepared were added in the medium for co-incubation, while 25 μL of PBS was added as the control. At specific time points, residual hydrogel was removed, and the remaining hydrogel and microsphere residues were washed off with serum-free medium twice. Then, 100 μL of MTT solution (5 mg/mL) was added to each well following the manufacturer's instructions and incubated at 37 °C for 3–4 h. After absorbing the co-culture solution, 700 μL of DMSO was added to dissolve the formed crystals. Next, 200 μL of supernatant was transferred from each well to another 96-well plate to detect absorbance at 490 nm and compare cell proliferation. Each group was measured in triplicate.

Additionally, the effects of P&G and P&G@LMs on NIH-3T3 proliferation were evaluated by live/dead staining using the same experimental method as before. According to the manufacturer's instructions, 250 μL of Calcein AM/PI detection solution was added to each well, and the cells were incubated at 37 °C for 10 min in the dark, and then imaging was performed using confocal microscopy. Each group was measured in triplicate.

4.17.3. In vitro evaluation of cell differentiation

Using NIH-3T3 cells to evaluate the effect of P&G and P&G@LMs hydrogel on the differentiation of fibroblasts into myofibroblasts. The method for making hydrogel discs was the same as before. Added 1 mL of NIH-3T3 cells at an initial density of $2*10^4$ cells per well into a confocal dish and incubate at 37 °C for 24 h to allow for cell adhesion. Then added TGF-β1 (5 ng/mL) to stimulate, and either 25 μL of P&G or 25 μL of P&G@LMs hydrogel discs prepared were added in the medium for co-incubation for 48h, while 25 μL of PBS was added as the control. Subsequently, according to the manufacturer's instructions, added anti-α-SMA antibody and fluorescent antibody, then imaging was performed using confocal microscopy. Each group was measured in triplicate.

4.18. Detection of antioxidant capacity of the hydrogel

The antioxidant efficiency of the hydrogel was assessed by scavenging 1,1-diphenyl-2-trinitrophenylhydrazine (DPPH) and nitroblue tetrazolium (NBT) free radicals. Briefly, put 14 mg of LMs, 300 μL of P&G, and 300 μL of P&G@LMs (containing equal amounts of LMs) into 2 mL of DPPH (100 μM) solution, respectively. Then the samples were incubated in a dark environment for 1 h. The wavelength at 517 nm was then measured using a UV–Vis spectrophotometer. Then put 14 mg of LMs, 300 μL of P&G, and 300 μL of P&G@LMs (containing equal amounts of LMs) into the PBS (pH 7.4) solution containing riboflavin (20 μM), methionine (20 μM), and NBT (75 μM). The mixed solution was irradiated with UV light for 3 min. Then the supernatants were extracted, and detected the absorbance at 560 nm. $O_2^{\cdot -}$ produced by UV light can reduce NBT to a blue formazan compound, with a maximum absorption peak at 560 nm. The ROS clearance formula was calculated as follows: clearance rate (%) = (A0 – A1)/A0*100 %, where A0 represents the absorbance of the substrate solution without hydrogel samples, and A1 represents the absorbance of the supernatant mixed with hydrogel samples. Each group was measured in triplicate.

4.19. Clearance of reactive oxygen species (ROS) from macrophages by hydrogel

The RAW264.7 cell line was used as the experimental cell model. RAW 264.7 cells (1 mL, $8*10^5$ cells/mL) were seeded into 6-well plates and cultured overnight. Subsequently, the medium was aspirated, and 1 mL of serum-free medium containing 10 μmol/L DCFH-DA was added to each well, followed by a 30-min incubation period. Afterward, 25 μL of P&G or P&G@LMs hydrogel discs, or 25 μL of PBS (prepared in advance), were added to the wells. Subsequently, 1 μL of 300 mM H_2O_2 was added per well (equivalent to 300 μM H_2O_2), while PBS without H_2O_2 served as the negative control group. Following co-incubation at 37 °C for 30 min, the residual medium, hydrogel, and microsphere residues were discarded, and cells were washed three times with PBS for 5 min each. Samples were then observed using a confocal laser microscope.

Simultaneously, levels of ROS were quantified using flow cytometry (FCM). The cell treatment protocol remained consistent with the aforementioned procedure. Cell suspensions ($1*10^6$ live cells) were collected from each tube and analyzed using FCM (CytoFLEX S, Beckman, America). An unstained control sample was also prepared as a compensation control to determine background levels. Prior to FCM detection, each tube of cell suspension was filtered through a 40 μm cell filter. Data were analyzed using FlowJo analysis software to record the percentage of positive events in FITC channels. Each group was measured in triplicate.

4.20. In vitro macrophage polarization

The RAW 264.7 cell line was used as the experimental cell model to assess the impact of P&G and P&G@LMs on CD86 and CD206 expression. Cell treatment included the LPS group (positive control), IL-4 group (negative control), LPS + P&G group, and LPS + P&G@LMs group. RAW 264.7 cells (1 mL, $8*10^5$ cells/mL) were seeded in 6-well plates, cultured overnight, and then subjected to different treatments. The positive control group was exposed to 1 mL of medium containing LPS (500 ng/mL) for 24 h, while the negative control group received 1 mL of medium containing IL-4 (50 ng/mL) for the same duration. The remaining two groups were exposed to 1 mL of medium containing LPS (500 ng/mL) along with 25 μL of either P&G or P&G@LMs hydrogel discs for 24 h. Subsequently, the residue of medium, hydrogels, and microspheres were removed, and cells were washed thrice with PBS for 5 min each time. Following the manufacturer's instructions, cells were incubated separately with PBS containing APC anti-mouse CD86 antibody and PE anti-mouse CD206/MMR antibody. FCM was utilized, and the data were analyzed using FlowJo analysis software to determine the percentage of positive channels. Each group was measured in triplicate.

For in vitro immunofluorescence staining, RAW 264.7 cells underwent the same treatment procedure before. And then cells underwent the following processing, which included fixing with 4 % paraformaldehyde, permeabilization with 0.5 % Triton X-100, and blocking using 1 % BSA. They were then incubated with a CD86-targeting or CD206-targeting rabbit polyclonal antibody (1:200, Proteintech) overnight, followed by 1 h period with AlexaFluor 488 goat anti-rabbit IgG secondary antibody (1:200, Proteintech) or CoraLite Plus 594 goat anti-rabbit IgG secondary antibody (1:200, Proteintech). Cell nucleus staining was done with DAPI, and visualization was achieved through confocal microscopy.

Concurrently, the DCFH-DA probe was employed to assess the level of ROS production in macrophages post-polarization, following the same cell treatment procedure. After PBS washing, 1 mL serum-free medium containing 10 μmol/L DCFH-DA was added to each well and incubated for 30 min, followed by three PBS washes. Laser confocal microscopy was employed for observation, and each group was measured in triplicate.

4.21. Gene expression of macrophages

Quantitative Polymerase Chain Reaction: q-PCR was carried out to test the influences of hydrogels on the gene expressions of IL-6, iNOS, Arg-1, and TGF-β1 in RAW 264.7 cells. Following the same cell treatment procedure before, total RNA was extracted using Trizol reagent (Biosharp) according to the protocol, and the concentration was determined by a NanoDrop 2000 spectrophotometer (Thermo Fisher). The following instructions were followed for reverse transcription of 1 μg total RNA using a First Strand cDNA Synthesis SuperMix for qPCR Kit (Yeasen), and q-PCR was conducted by Hieff qPCR SYBR Green Master Mix (Yeasen). The $2-\Delta\Delta Ct$ method was employed to analyze the relative gene expression. The sequences of the primers were listed in Table S1 (Supporting Information).

4.22. Cell migration evaluation

The migration of epidermal cells was analyzed using the scratch assay, with HaCaT cells serving as the experimental cells. To explain simply, HaCaT cells (1 mL, $6*10^5$ cells/mL) were first seeded into 12-well plates and cultured for 24 h until reaching 80–90 % confluency. Subsequently, a 200 μL pipette tip was used to create a uniform scratch on the cell layer at the bottom of the plate. After two washes with PBS, serum-free medium was added, and the remaining cells were photographed. Following this, 25 μL of P&G, 25 μL of P&G@LMs hydrogel discs, or 25 μL of PBS were added to each well, along with 1 μL of 100 mM H_2O_2 (equivalent to 100 μM H_2O_2). The negative control group received PBS without H_2O_2. After co-incubation for 24 and 48 h, the residual hydrogel and microsphere residues were removed, and cells were washed off twice with PBS before being photographed under a microscope. ImageJ software was utilized to analyze the migration of HaCaT cells, with the calculation formula as follows: scratch healing (%) = (S0-St)/S0*100 %, where S0 represents the initial scratch area, and St represents the scratch area after 24 and 48 h. Each group was measured in triplicate.

4.23. Wound healing and scar area assessment

Based on previous studies, the animal studies have shown that oral administration of ACEI at a dosage of 10 mg/kg bodyweight/day (equivalent to 0.25 mg/25g bodyweight/day) in mice with an average weight of 25g has been shown to inhibit scar formation after wound healing [31,69]. Considering the advantages of topical medications, such as their potential to reduce systemic side effects, we opted for a slightly higher drug concentration than that used in previous studies for

our animal experiments. We mixed 100 mg of LMs with 900 μL of P&G hydrogel to prepare 50 μL of P&G@LMs discs for application on mouse wounds. Each 50 μL of P&G@LMs disc contained approximately 0.25 mg of ACEI, and bilateral wounds received about 0.5 mg of ACEI in total, equivalent to 0.5 mg/25g bodyweight/8 days. And 100 mg of LMs was evenly mixed with 900 μL of PBS to form a solution of LMs. All animal experimental protocols were approved by the Ethics Committee for Animal Use of Sir Run Run Shaw Hospital, School of Medicine, Zhejiang University (Protocol number SRRSH202302079). C57BL/6 male mice, 8 weeks old (weighing approximately 23–25g), were housed indoors under constant temperature (55%–65 %) and humidity, provided with a standard diet, and maintained on a 12-h light-dark cycle. Mice were treated with 3 % isoflurane to induce anesthesia and 1.5 % isoflurane to maintain anesthesia. After depilation of their back hair using depilatory cream, a smooth area measuring about 3 cm*4 cm was exposed. Following disinfection with 75 % alcohol, the spine of the back of mice was taken as the center line, and a circular excision with a diameter of 8 mm was made at 4 mm on both sides of the center line. The entire skin and subcutaneous tissue were excised, and silicone rings were sutured around the incision using 5-0 silk thread. After surgery, the wound and surrounding area were disinfected with iodine using a cotton swab. Subsequently, the mice were randomly divided into four groups: PBS (control), P&G, LMs, and P&G@LMs. Each group received 50 μL of their respective treatments applied to the wound, followed by sterile dressing and gentle compression with hypoallergenic adhesive tape. Images of the wounds were captured at days 0, 5, 10, and 15 post-injury. Digital images were analyzed using ImageJ software to calculate the wound closure percentage using the formula: Wound closure rate (%) = (A0-At)/A0*100 %, where A0 represents the initial wound area and At represents the wound area at each time point after injury or the final scar area. Each group was measured in triplicate.

4.24. Histological, immunohistochemical and immunofluorescence assessments

Scar tissue along with adjacent normal skin and major organs (heart, liver, spleen, lungs, and kidneys) were excised on the 15th postoperative day and then fixed in 4 % paraformaldehyde for subsequent histological, immunohistochemical, and immunofluorescence analysis. In brief, the excised and fixed tissues were dehydrated, embedded in paraffin wax, sectioned into 5 μm slices, and stained. Skin sections were stained with hematoxylin and eosin (H&E), Picrosirius red as well as the Masson tricolor stain kit following the manufacturer's instructions. Following that, sections were immunostained with anti-TGF-β1, anti-α-SMA, anti-TNF-α, anti-CD86, and anti-CD206 antibodies. Major organs were stained with H&E. The sections were examined using a fluorescence microscope and a digital microscope. Three or four different random images from each group were subjected to quantitative analysis.

5. Statistical analysis

All experiments were performed at least three times and the results were expressed as mean ± standard deviation (SD). The level of statistical significance was determined using Prism 10.0 through two-tailed Student's t-test or one-way analysis of variance (ANOVA). Error bars represent the mean ± standard deviation. *$P < 0.05$; **$P < 0.01$; ***$P < 0.001$; ****$P < 0.0001$; NS, not statistically significant. Statistic differences were considered significantly at $P < 0.05$.

CRediT authorship contribution statement

Tao Zhang: Writing – review & editing, Writing – original draft, Visualization, Software, Methodology, Investigation, Data curation, Formal analysis, Conceptualization. **Xin-Cao Zhong:** Methodology, Formal analysis, Visualization, Writing – review & editing, Investigation. **Zi-Xuan Feng:** Data curation, Formal analysis, Software, Visualization, Writing – review & editing. **Xiao-Ying Lin:** Resources, Project administration, Funding acquisition, Data curation. **Chun-Ye Chen:** Visualization, Validation, Software. **Xiao-Wei Wang:** Resources, Project administration, Funding acquisition. **Kai Guo:** Methodology, Investigation, Software. **Yi Wang:** Supervision, Software, Visualization. **Jun Chen:** Formal analysis, Data curation, Conceptualization, Methodology. **Yong-Zhong Du:** Methodology, Conceptualization, Data curation, Formal analysis. **Ze-Ming Zhuang:** Writing – review & editing, Visualization, Validation, Software, Methodology, Investigation. **Yong Wang:** Writing – review & editing, Supervision, Investigation, Data curation, Conceptualization. **Wei-Qiang Tan:** Resources, Project administration, Funding acquisition, Conceptualization, Data curation, Methodology, Supervision, Validation, Writing – original draft, Writing – review & editing.

Ethics approval and consent to participate

All animal experimental protocols were approved by the Ethics Committee for Animal Use of Sir Run Run Shaw Hospital, School of Medicine, Zhejiang University (Protocol number SRRSH202302079). Animal experiments were conducted in accordance with the Guidelines for Animal Care and Use Committee of Zhejiang University.

Data availability statement

The data presented in the study are included in the article, further inquiries can be directed to the corresponding author.

Declaration of competing interest

The authors declare that they have no known competing financial interests or personal relationships that could have appeared to influence the work reported in this paper.

Acknowledgements

This work was supported by grants from Zhejiang Provincial Medical and Healthy Science Foundation of China (No. 2023RC183, 2023RC123, and 2024KY110), National Natural Science Foundation of China (No. 82172206). We sincerely thank Professor Jun Chen from the MOE Key Laboratory of Biosystems Homeostasis & Protection, College of Life Sciences, Zhejiang University, and Professor Yong-Zhong Du from the Institute of Pharmaceutics, College of Pharmaceutical Sciences, Zhejiang University, for their experimental support and highly instructive suggestions. And we thank Xiaoli Hong and Chao Bi from the Core Facilities, Zhejiang University School of Medicine for their technical support. All authors have approved the final version of this manuscript.

Appendix A. Supplementary data

Supplementary data to this article can be found online at https://doi.org/10.1016/j.bioactmat.2024.11.028.

References

[1] G.C. Gurtner, S. Werner, Y. Barrandon, M.T. Longaker, Wound repair and regeneration, Nature 453 (7193) (2008) 314–321.
[2] T. Zhang, X.-F. Wang, Z.-C. Wang, D. Lou, Q.-Q. Fang, Y.-Y. Hu, W.-Y. Zhao, L.-Y. Zhang, L.-H. Wu, W.-Q. Tan, Current potential therapeutic strategies targeting the TGF-β/Smad signaling pathway to attenuate keloid and hypertrophic scar formation, Biomed. Pharmacother. 129 (2020).
[3] E. Bellu, S. Medici, D. Coradduzza, S. Cruciani, E. Amler, M. Maioli, Nanomaterials in skin regeneration and Rejuvenation, Int. J. Mol. Sci. 22 (13) (2021).
[4] M. Monavarian, S. Kader, S. Moeinzadeh, E. Jabbari, Regenerative scar-free skin wound healing, Tissue Eng. B Rev. 25 (4) (2019) 294–311.
[5] C.E. Berry, M. Downer, A.G. Morgan, M. Griffin, N.E. Liang, L. Kameni, J.B. Laufey Parker, J. Guo, M.T. Longaker, D.C. Wan, The effects of mechanical force on fibroblast behavior in cutaneous injury, Frontiers in Surgery 10 (2023).

[6] F.S. Frech, L. Hernandez, R. Urbonas, G.A. Zaken, I. Dreyfuss, K. Nouri, Hypertrophic scars and keloids: advances in treatment and review of established therapies, Am. J. Clin. Dermatol. 24 (2) (2023) 225–245.
[7] Y. Gao, A. Sarode, N. Kokoroskos, A. Ukidve, Z. Zhao, S. Guo, R. Flaumenhaft, A. S. Gupta, N. Saillant, S. Mitragotri, A polymer-based systemic hemostatic agent, Sci. Adv. 6 (31) (2020) eaba0588.
[8] M. Sharifiaghdam, E. Shaabani, R. Faridi-Majidi, S.C. De Smedt, K. Braeckmans, J. C. Fraire, Macrophages as a therapeutic target to promote diabetic wound healing, Mol. Ther. 30 (9) (2022) 2891–2908.
[9] S.A. Eming, T.A. Wynn, P. Martin, Inflammation and metabolism in tissue repair and regeneration, Science 356 (6342) (2017) 1026–1030.
[10] Y. Qian, Y. Zheng, J. Jin, X. Wu, K. Xu, M. Dai, Q. Niu, H. Zheng, X. He, J. Shen, Immunoregulation in diabetic wound repair with a photoenhanced glycyrrhizic acid hydrogel scaffold, Adv. Mater. 34 (29) (2022).
[11] P. Rousselle, F. Braye, G. Dayan, Re-epithelialization of adult skin wounds: cellular mechanisms and therapeutic strategies, Adv. Drug Deliv. Rev. 146 (2019) 344–365.
[12] K. Wu, D. Zhu, X. Dai, W. Wang, X. Zhong, Z. Fang, C. Peng, X. Wei, H. Qian, X. Chen, X. Wang, Z. Zha, L. Cheng, Bimetallic oxide Cu1.5Mn1.5O4 cage-like frame nanospheres with triple enzyme-like activities for bacterial-infected wound therapy, Nano Today 43 (2022).
[13] N.C. Henderson, F. Rieder, T.A. Wynn, Fibrosis: from mechanisms to medicines, Nature 587 (7835) (2020) 555–566.
[14] M. Lodyga, E. Cambridge, H.M. Karvonen, P. Pakshir, B. Wu, S. Boo, M. Kiebalo, R. Kaarteenaho, M. Glogauer, M. Kapoor, K. Ask, B. Hinz, Cadherin-11-mediated adhesion of macrophages to myofibroblasts establishes a profibrotic niche of active TGF-beta, Sci. Signal. 12 (564) (2019).
[15] F.S. Younesi, A.E. Miller, T.H. Barker, F.M.V. Rossi, B. Hinz, Fibroblast and myofibroblast activation in normal tissue repair and fibrosis, Nat. Rev. Mol. Cell Biol. 25 (8) (2024) 617–638.
[16] M. Zhao, L. Wang, M. Wang, S. Zhou, Y. Lu, H. Cui, A.C. Racanelli, L. Zhang, T. Ye, B. Ding, B. Zhang, J. Yang, Y. Yao, Targeting fibrosis: mechanisms and clinical trials, Signal Transduct. Targeted Ther. 7 (1) (2022).
[17] X. Qi, E. Cai, Y. Xiang, C. Zhang, X. Ge, J. Wang, Y. Lan, H. Xu, R. Hu, J. Shen, An immunomodulatory hydrogel by hyperthermia-assisted self-cascade glucose depletion and ROS scavenging for diabetic foot ulcer wound therapeutics, Adv. Mater. 35 (48) (2023).
[18] J. Sun, W. Jia, H. Qi, J. Huo, X. Liao, Y. Xu, J. Wang, Z. Sun, Y. Liu, J. Liu, M. Zhen, C. Wang, C. Bai, An antioxidative and active shrinkage hydrogel integratedly promotes Re-epithelization and skin constriction for enhancing wound closure, Adv. Mater. 36 (21) (2024).
[19] L. Sun, J. Zhou, J. Lai, X. Zheng, H. Wang, B. Lu, R. Huang, L.M. Zhang, Novel natural polymer-based hydrogel patches with janus asymmetric-adhesion for emergency hemostasis and wound healing, Adv. Funct. Mater. (2024).
[20] D. Okwan-Duodu, V. Datta, X.Z. Shen, H.S. Goodridge, E.A. Bernstein, S. Fuchs, G. Y. Liu, K.E. Bernstein, Angiotensin-converting enzyme overexpression in mouse myelomonocytic cells augments resistance to Listeria and methicillin-resistant Staphylococcus aureus, J. Biol. Chem. 285 (50) (2010) 39051–39060.
[21] X.Z. Shen, P. Li, D. Weiss, S. Fuchs, H.D. Xiao, J.A. Adams, I.R. Williams, M. R. Capecchi, W.R. Taylor, K.E. Bernstein, Mice with enhanced macrophage angiotensin-converting enzyme are resistant to melanoma, Am. J. Pathol. 170 (6) (2007) 2122–2134.
[22] J. Boskabadi, V.R. Askari, M. Hosseini, M.H. Boskabady, Immunomodulatory properties of captopril, an ACE inhibitor, on LPS-induced lung inflammation and fibrosis as well as oxidative stress, Inflammopharmacology 27 (3) (2018) 639–647.
[23] M. Suzuki, S. Teramoto, H. Katayama, E. Ohga, T. Matsuse, Y. Ouchi, Effects of angiotensin-converting enzyme (ACE) inhibitors on oxygen radical production and generation by murine lung alveolar macrophages, J. Asthma 36 (8) (2009) 665–670.
[24] L. Wu, K. Chen, J. Xiao, J. Xin, L. Zhang, X. Li, L. Li, J. Si, L. Wang, K. Ma, Angiotensin II induces RAW264.7 macrophage polarization to the M1-type through the connexin 43/NF-κB pathway, Mol. Med. Rep. (2020).
[25] S. Medjebar, C. Truntzer, A. Perrichet, E. Limagne, J.-D. Fumet, C. Richard, A. Elkrief, B. Routy, C. Rébé, F. Ghiringhelli, Angiotensin-converting enzyme (ACE) inhibitor prescription affects non-small-cell lung cancer (NSCLC) patients response to PD-1/PD-L1 immune checkpoint blockers, OncoImmunology 9 (1) (2020).
[26] S. Bhandari, S. Mehta, A. Khwaja, J.G.F. Cleland, N. Ives, E. Brettell, M. Chadburn, P. Cockwell, Renin–angiotensin system inhibition in advanced chronic kidney disease, N. Engl. J. Med. 387 (22) (2022) 2021–2032.
[27] K.Y. Shim, Y.W. Eom, M.Y. Kim, S.H. Kang, S.K. Baik, Role of the renin-angiotensin system in hepatic fibrosis and portal hypertension, Kor. J. Intern. Med. 33 (3) (2018) 453–461.
[28] Q.-Q. Fang, X.-F. Wang, W.-Y. Zhao, C.-Y. Chen, M.-X. Zhang, B.-H. Shi, L.-Y. Zhang, W.-Q. Tan, The source of ACE during scar formation is from both bone marrow and skin tissue, Faseb. J. 32 (9) (2018) 5199–5208.
[29] K. Hedayatyanfard, N.S. Haddadi, S.A. Ziai, H. Karim, F. Niazi, U.M. Steckelings, B. Habibi, A. Modarressi, A.R. Dehpour, The renin-angiotensin system in cutaneous hypertrophic scar and keloid formation, Exp. Dermatol. 29 (9) (2020) 902–909.
[30] F. Jiang, J. Yang, Y. Zhang, M. Dong, S. Wang, Q. Zhang, F.F. Liu, K. Zhang, C. Zhang, Angiotensin-converting enzyme 2 and angiotensin 1–7: novel therapeutic targets, Nat. Rev. Cardiol. 11 (7) (2014) 413–426.
[31] W.Q. Tan, Q.Q. Fang, X.Z. Shen, J.F. Giani, T.V. Zhao, P. Shi, L.Y. Zhang, Z. Khan, Y. Li, L. Li, J.H. Xu, E.A. Bernstein, K.E. Bernstein, Angiotensin-converting enzyme inhibitor works as a scar formation inhibitor by down-regulating Smad and TGF-β-activated kinase 1 (TAK1) pathways in mice, Br. J. Pharmacol. 175 (22) (2018) 4239–4252.
[32] B. Zheng, Q.-Q. Fang, X.-F. Wang, B.-H. Shi, W.-Y. Zhao, C.-Y. Chen, M.-X. Zhang, L.-Y. Zhang, Y.-Y. Hu, P. Shi, L. Ma, W.-Q. Tan, The effect of topical ramipril and losartan cream in inhibiting scar formation, Biomed. Pharmacother. 118 (2019).
[33] Y. Su, B. Zhang, R. Sun, W. Liu, Q. Zhu, X. Zhang, R. Wang, C. Chen, PLGA-based biodegradable microspheres in drug delivery: recent advances in research and application, Drug Deliv. 28 (1) (2021) 1397–1418.
[34] M.B. Giles, J.K.Y. Hong, Y. Liu, J. Tang, T. Li, A. Beig, A. Schwendeman, S. P. Schwendeman, Efficient aqueous remote loading of peptides in poly(lactic-co-glycolic acid), Nat. Commun. 13 (1) (2022).
[35] J. Sun, L. Xiao, B. Li, K. Zhao, Z. Wang, Y. Zhou, C. Ma, J. Li, H. Zhang, A. Herrmann, K. Liu, Genetically engineered polypeptide adhesive coacervates for surgical applications, Angew. Chem. Int. Ed. 60 (44) (2021) 23687–23694.
[36] G.M. Taboada, K. Yang, M.J.N. Pereira, S.S. Liu, Y. Hu, J.M. Karp, N. Artzi, Y. Lee, Overcoming the translational barriers of tissue adhesives, Nat. Rev. Mater. 5 (4) (2020) 310–329.
[37] J. Li, D.J. Mooney, Designing hydrogels for controlled drug delivery, Nat. Rev. Mater. 1 (12) (2016).
[38] S. Bian, L. Hao, X. Qiu, J. Wu, H. Chang, G.M. Kuang, S. Zhang, X. Hu, Y. Dai, Z. Zhou, F. Huang, C. Liu, X. Zou, W. Liu, W.W. Lu, H. Pan, X. Zhao, An injectable rapid-adhesion and anti-swelling adhesive hydrogel for hemostasis and wound sealing, Adv. Funct. Mater. 32 (46) (2022).
[39] S. Li, C. Yang, J. Li, C. Zhang, L. Zhu, Y. Song, Y. Guo, R. Wang, D. Gan, J. Shi, P. Ma, F. Gao, H. Su, Progress in pluronic F127 derivatives for application in wound healing and repair, Int. J. Nanomed. 18 (2023) 4485–4505.
[40] L. Song, B. Zhang, G. Gao, C. Xiao, G. Li, Single component Pluronic F127-lipoic acid hydrogels with self-healing and multi-responsive properties, Eur. Polym. J. 115 (2019) 346–355.
[41] C. Ligorio, A. Mata, Synthetic extracellular matrices with function-encoding peptides, Nature Reviews Bioengineering 1 (7) (2023) 518–536.
[42] O. Hasturk, K.E. Jordan, J. Choi, D.L. Kaplan, Enzymatically crosslinked silk and silk-gelatin hydrogels with tunable gelation kinetics, mechanical properties and bioactivity for cell culture and encapsulation, Biomaterials 232 (2020).
[43] G. Li, S. Liu, Y. Chen, J. Zhao, H. Xu, J. Weng, F. Yu, A. Xiong, A. Uddutula, D. Wang, P. Liu, Y. Chen, H. Zeng, An injectable liposome-anchored teriparatide incorporated gallic acid-grafted gelatin hydrogel for osteoarthritis treatment, Nat. Commun. 14 (1) (2023).
[44] Z. Zhao, G. Li, H. Ruan, K. Chen, Z. Cai, G. Lu, R. Li, L. Deng, M. Cai, W. Cui, Capturing magnesium ions via microfluidic hydrogel microspheres for promoting cancellous bone regeneration, ACS Nano 15 (8) (2021) 13041–13054.
[45] K. A, L. A, Mechanical behaviour of skin: a review, J. Mater. Sci. Eng. 5 (4) (2016).
[46] Y. Zhang, L. Tao, S. Li, Y. Wei, Synthesis of multiresponsive and dynamic chitosan-based hydrogels for controlled release of bioactive molecules, Biomacromolecules 12 (8) (2011) 2894–2901.
[47] Q. Hu, N. Xie, K. Liao, J. Huang, Q. Yang, Y. Zhou, Y. Liu, K. Deng, An injectable thermosensitive Pluronic F127/hyaluronic acid hydrogel loaded with human umbilical cord mesenchymal stem cells and asiaticoside microspheres for uterine scar repair, Int. J. Biol. Macromol. 219 (2022) 96–108.
[48] T. Hozumi, T. Kageyama, S. Ohta, J. Fukuda, T. Ito, Injectable hydrogel with slow degradability composed of gelatin and hyaluronic acid cross-linked by schiff's base formation, Biomacromolecules 19 (2) (2018) 288–297.
[49] Y. Li, H. Zhang, Q. Liu, FT-IR spectroscopy and DFT calculation study on the solvent effects of benzaldehyde in organic solvents, Spectrochim. Acta Mol. Biomol. Spectrosc. 86 (2012) 51–55.
[50] L. Mei, D. Zhang, H. Shao, Y. Hao, T. Zhang, W. Zheng, Y. Ji, P. Ling, Y. Lu, Q. Zhou, Injectable and self-healing probiotics-loaded hydrogel for promoting superbacteria-infected wound healing, ACS Appl. Mater. Interfaces 14 (18) (2022) 20538–20550.
[51] X. Na, W. Zhou, T. Li, D. Hong, J. Li, G. Ma, Preparation of double-emulsion-templated microspheres with controllable porous structures by premix membrane emulsification, Particuology 44 (2019) 22–27.
[52] H.K. Makadia, S.J. Siegel, Poly lactic-co-glycolic acid (PLGA) as biodegradable controlled drug delivery carrier, Polymers 3 (3) (2011) 1377–1397.
[53] H. Tan, J. Wu, L. Lao, C. Gao, Gelatin/chitosan/hyaluronan scaffold integrated with PLGA microspheres for cartilage tissue engineering, Acta Biomater. 5 (1) (2009) 328–337.
[54] D. Correa-Gallegos, D. Jiang, S. Christ, P. Ramesh, H. Ye, J. Wannemacher, S. Kalgudde Gopal, Q. Yu, M. Aichler, A. Walch, U. Mirastschijski, T. Volz, Y. Rinkevich, Patch repair of deep wounds by mobilized fascia, Nature 576 (7786) (2019) 287–292.
[55] D. Jiang, D. Correa-Gallegos, S. Christ, A. Stefanska, J. Liu, P. Ramesh, V. Rajendran, M.M. De Santis, D.E. Wagner, Y. Rinkevich, Two succeeding fibroblastic lineages drive dermal development and the transition from regeneration to scarring, Nat. Cell Biol. 20 (4) (2018) 422–431.
[56] S. Chatterjee, P.C.-l. Hui, C.-w. Kan, W. Wang, Dual-responsive (pH/temperature) Pluronic F-127 hydrogel drug delivery system for textile-based transdermal therapy, Sci. Rep. 9 (1) (2019).
[57] R.T. Polez, M. Morits, C. Jonkergouw, J. Phiri, J.J. Valle-Delgado, M.B. Linder, T. Maloney, O.J. Rojas, M. Österberg, Biological activity of multicomponent bio-hydrogels loaded with tragacanth gum, Int. J. Biol. Macromol. 215 (2022) 691–704.
[58] J. Chen, H. Zhu, J. Xia, Y. Zhu, C. Xia, Z. Hu, Y. Jin, J. Wang, Y. He, J. Dai, Z. Hu, High-performance multi-dynamic bond cross-linked hydrogel with spatiotemporal siRNA delivery for gene–cell combination therapy of intervertebral disc degeneration, Adv. Sci. 10 (17) (2023).
[59] W. Feng, Z. Wang, Tailoring the swelling-shrinkable behavior of hydrogels for biomedical applications, Adv. Sci. 10 (28) (2023).

[60] S. Pourshahrestani, E. Zeimaran, N.A. Kadri, N. Mutlu, A.R. Boccaccini, Polymeric hydrogel systems as emerging biomaterial platforms to enable hemostasis and wound healing, Adv. Healthcare Mater. 9 (20) (2020).
[61] J.P. Junker, R.A. Kamel, E.J. Caterson, E. Eriksson, Clinical impact upon wound healing and inflammation in moist, wet, and dry environments, Adv. Wound Care 2 (7) (2013) 348–356.
[62] A. Gupta, M. Kowalczuk, W. Heaselgrave, S.T. Britland, C. Martin, I. Radecka, The production and application of hydrogels for wound management: a review, Eur. Polym. J. 111 (2019) 134–151.
[63] I. Standard, Biological Evaluation of Medical Devices—Part 5: Tests for in Vitro Cytotoxicity, International Organization for Standardization, Geneve, Switzerland, 2009.
[64] S. Willenborg, D.E. Sanin, A. Jais, X. Ding, T. Ulas, J. Nüchel, M. Popović, T. MacVicar, T. Langer, J.L. Schultze, A. Gerbaulet, A. Roers, E.J. Pearce, J. C. Brüning, A. Trifunovic, S.A. Eming, Mitochondrial metabolism coordinates stage-specific repair processes in macrophages during wound healing, Cell Metabol. 33 (12) (2021) 2398–2414.e9.
[65] A.E.K. Loo, R. Ho, B. Halliwell, Mechanism of hydrogen peroxide-induced keratinocyte migration in a scratch-wound model, Free Radic. Biol. Med. 51 (4) (2011) 884–892.
[66] B. Perillo, M. Di Donato, A. Pezone, E. Di Zazzo, P. Giovannelli, G. Galasso, G. Castoria, A. Migliaccio, ROS in cancer therapy: the bright side of the moon, Exp. Mol. Med. 52 (2) (2020) 192–203.
[67] M. Redza-Dutordoir, D.A. Averill-Bates, Activation of apoptosis signalling pathways by reactive oxygen species, Biochim. Biophys. Acta Mol. Cell Res. 1863 (12) (2016) 2977–2992.
[68] Y. Wang, Y. Zhang, Y.-P. Yang, M.-Y. Jin, S. Huang, Z.-M. Zhuang, T. Zhang, L.-L. Cao, X.-Y. Lin, J. Chen, Y.-Z. Du, J. Chen, W.-Q. Tan, Versatile dopamine-functionalized hyaluronic acid-recombinant human collagen hydrogel promoting diabetic wound healing via inflammation control and vascularization tissue regeneration, Bioact. Mater. 35 (2024) 330–345.
[69] Q.-Q. Fang, X.-F. Wang, W.-Y. Zhao, S.-L. Ding, B.-H. Shi, Y. Xia, H. Yang, L.-H. Wu, C.-Y. Li, W.-Q. Tan, Angiotensin-converting enzyme inhibitor reduces scar formation by inhibiting both canonical and noncanonical TGF-β1 pathways, Sci. Rep. 8 (1) (2018).
[70] N.A.J. Cremers, M. Suttorp, M.M. Gerritsen, R.J. Wong, C. van Run-van Breda, G. M. van Dam, K.M. Brouwer, A.M. Kuijpers-Jagtman, C.E.L. Carels, D.M.S. Lundvig, F.A.D.T.G. Wagener, Mechanical stress changes the complex interplay between HO-1, inflammation and fibrosis, during excisional wound repair, Front. Med. 2 (2015).
[71] D.O. Son, B. Hinz, A rodent model of hypertrophic ScarringHypertrophic scarring: SplintingSplinting of rat wounds, in: B. Hinz, D. Lagares (Eds.), Myofibroblasts: Methods and Protocols, Springer US, New York, NY, 2021, pp. 405–417.
[72] D. Lagares, B. Hinz, Animal and human models of tissue RepairTissuerepair and fibrosis: an introduction, in: B. Hinz, D. Lagares (Eds.), Myofibroblasts: Methods and Protocols, Springer US, New York, NY, 2021, pp. 277–290.
[73] X. Wang, J. Ge, E.E. Tredget, Y. Wu, The mouse excisional wound splinting model, including applications for stem cell transplantation, Nat. Protoc. 8 (2) (2013) 302–309.
[74] J. Gao, Z. Guo, Y. Zhang, Y. Liu, F. Xing, J. Wang, X. Luo, Y. Kong, G. Zhang, Age-related changes in the ratio of Type I/III collagen and fibril diameter in mouse skin, Regenerative Biomaterials 10 (2023).
[75] D. Singh, V. Rai, D.K. Agrawal, Regulation of collagen I and collagen III in tissue injury and regeneration, Cardiology and Cardiovascular Medicine 7 (1) (2023).
[76] W. Wang, L. Chen, Y. Zhang, H. Wang, D. Dong, J. Zhu, W. Fu, T. Liu, Adipose-derived stem cells enriched with therapeutic mRNA TGF-β3 and IL-10 synergistically promote scar-less wound healing in preclinical models, Bioengineering & Translational Medicine 9 (2) (2023).